

JGR Space Physics

RESEARCH ARTICLE

10.1029/2023JA032113

Key Points:

- Using a hybrid model, we provide three-dimensional context for plasma and magnetic field observations from the Juno PJ34 flyby of Ganymede
- Escaping heavy ions from Ganymede's ionosphere cause subtle, but discernible modifications to the magnetic field in the vicinity of the moon
- Ganymede's sub-Jovian magnetopause is susceptible to Kelvin-Helmholtz instabilities, causing the location of the boundary layer to oscillate

Correspondence to:

A. Stahl,
astahl3@gatech.edu

Citation:

Stahl, A., Addison, P., Simon, S., & Liuzzo, L. (2023). A model of Ganymede's magnetic and plasma environment during the Juno PJ34 flyby. *Journal of Geophysical Research: Space Physics*, 128, e2023JA032113. <https://doi.org/10.1029/2023JA032113>

Received 22 SEP 2023
Accepted 15 NOV 2023

A Model of Ganymede's Magnetic and Plasma Environment During the Juno PJ34 Flyby

Aaron Stahl^{1,2} , Peter Addison¹ , Sven Simon^{1,2} , and Lucas Liuzzo³ 

¹School of Earth and Atmospheric Sciences, Georgia Institute of Technology, Atlanta, GA, USA, ²School of Physics, Georgia Institute of Technology, Atlanta, GA, USA, ³Space Sciences Laboratory, University of California, Berkeley, Berkeley, CA, USA

Abstract Using a hybrid model (kinetic ions, fluid electrons), we provide context for plasma and magnetic field observations from Juno's PJ34 flyby of Ganymede on 07 June 2021. We consider five model configurations that successively increase the complexity of Ganymede's atmosphere and ionosphere by including additional particle species and ionization mechanisms. We examine the density and flow patterns of pick-up ions with small (H_2^+), intermediate (H_2O^+), and large (O_2^+) masses in Ganymede's interaction region. The results are validated by comparing the modeled magnetic field and ion densities against time series from Juno's magnetometer and plasma instruments. Our major findings are: (a) Ganymede's internal dipole dominated the magnetic field signature observed inside the moon's magnetosphere, while plasma currents shaped the field perturbations within the "wake" region detected along the Jupiter-averaged magnetopause. (b) Ganymede's pick-up tail leaves a subtle, but clearly discernible imprint in the magnetic field downstream of the moon. (c) Heavy pick-up ions dominate ionospheric outflow and form a tail with steep outer boundaries. (d) During the flyby, the position of Ganymede's Jupiter-facing magnetopause varied in time due to Kelvin-Helmholtz waves traveling along the boundary layer. As such, the location of the Jupiter-facing magnetopause observed by Juno represents only a single snapshot of this time-dependent process. (e) Ionospheric hydrogen ions are partially generated outside of Ganymede's magnetopause, forming a dilute H_2^+ corona that surrounds the moon's magnetosphere. (f) Most H_2O^+ ions are produced at low latitudes where field lines are closed, resulting in a very dilute pick-up tail for this species.

1. Introduction

Jupiter's third Galilean moon, Ganymede, is the largest moon in the solar system with a radius of $R_G = 2,634.1$ km and orbits its parent planet at a distance of 15 Jupiter radii ($R_J = 71,492$ km). Ganymede's orbit is nearly circular and coincides with the planet's rotational equatorial plane. The moon is embedded within Jupiter's expansive magnetosphere, whose magnetopause possesses a ramside stand-off distance of at least $45 R_J$ (e.g., Connerney, Adriani, et al., 2017; Connerney, Benn, et al., 2017; Joy et al., 2002). Ganymede is the only satellite known to possess an intrinsic global magnetic field (Gurnett et al., 1996; Kivelson et al., 1996). This intrinsic field is largely dipolar (Kivelson et al., 2002; Weber et al., 2022) and driven by dynamo action in a metallic molten core (Anderson et al., 1996; Schubert et al., 1996). It generates an equatorial surface field magnitude of 719 nT, which is at least 6 times that of the ambient Jovian magnetospheric field (Kivelson et al., 2002). Jupiter's dipole moment is tilted at 9.6° relative to its spin axis, causing the Jovian magnetic equator to sweep over the moon twice each synodic rotation period (about 10 hr, see Kivelson et al. (2004) or Saur et al. (2010)). The time-varying horizontal magnetospheric field component experienced by Ganymede reaches magnitudes of up to about 80 nT. Its oscillations generate an induced field from the subsurface ocean located 150–250 km beneath Ganymede's surface (Kivelson et al., 2002; Saur et al., 2015). The magnitude of this induced field is at most 6% that of the intrinsic field at the moon's surface (Kivelson et al., 2002).

Ganymede has a dilute atmosphere predominantly composed of O_2 at low altitudes and H_2 above a few hundred kilometers (e.g., Leblanc et al., 2017; Marconi, 2007). High-sensitivity spectral images acquired by the Hubble Space Telescope (HST) recently revealed H_2O in Ganymede's dayside atmosphere, suggesting it to be the dominant species around the subsolar point (Leblanc et al., 2023; Roth et al., 2021). Analysis of Lyman- α emissions observed by HST also recently confirmed the presence of an extended hydrogen corona around the moon (Alday et al., 2017; Roth et al., 2023). Electron density profiles derived from plasma wave observations and radio occultation measurements suggest that Ganymede is surrounded by an ionosphere, consisting largely of O_2^+ and H_2^+ as

©2023. The Authors.

This is an open access article under the terms of the [Creative Commons Attribution License](#), which permits use, distribution and reproduction in any medium, provided the original work is properly cited.

well as minor contributions from O⁺ and H⁺ (e.g., Buccino et al., 2022; Carnielli et al., 2019; Eviatar, Vasylunas, & Gurnett, 2001; Eviatar et al., 2000). The moon also exhibits auroral emissions driven by electron excitation of atmospheric molecules. These emissions are primarily observed along two oval-shaped regions enclosing Ganymede's polar regions at high latitudes (Feldman et al., 2000; Hall et al., 1998; McGrath et al., 2013; Molyneux et al., 2018). Oscillations in the locations of the auroral ovals on the same time scale as Jupiter's synodic rotation were observed by HST. These oscillations were used to show the presence of an inductive response from the moon's subsurface ocean (Saur et al., 2015).

The ambient plasma environment at Ganymede is populated with charged particles primarily originating from Io (Bagenal et al., 2016; Kim et al., 2020). These particles are transported radially outward through flux tube interchange (Bagenal & Delamere, 2011) and co-rotate at 80% of Jupiter's rotation velocity near Ganymede's orbit (Williams, Mauk, & McEntire, 1997; Williams, Mauk, McEntire, Roelof, et al., 1997). The bulk velocity of the magnetospheric plasma exceeds the moon's Keplerian speed by about an order of magnitude. Therefore, the flow overtakes Ganymede with a relative velocity of 120–160 km/s (Kivelson et al., 2004). The upstream magnetospheric plasma is sub-Alfvénic and sub-magnetosonic (e.g., Jia & Kivelson, 2021; Kivelson et al., 2004), so no bow shock is formed upstream of Ganymede. The moon is tidally locked with Jupiter, resulting in the same hemisphere always oriented toward the upstream flow. At Ganymede's orbit, the Jovian magnetospheric plasma is confined to an equatorial sheet with a number density $n(d) = n_0 \exp[-(d/H)^2]$, where d is the distance to the center of the sheet, $H \approx 3R_J$, and $n_0 \approx 10^7 \text{ m}^{-3}$ (Bagenal & Delamere, 2011). This plasma sheet lies between Jupiter's magnetic and centrifugal equators, imparting a synodic periodicity to Ganymede's environment: the plasma density varies by up to a factor of 5 as the sheet passes over the moon (Jia & Kivelson, 2021).

Ganymede's strong intrinsic field carves out a mini-magnetosphere within Jupiter's magnetosphere, decelerating the incident plasma flow in the orbital trailing hemisphere and diverting it around the moon's internal field (e.g., Gurnett et al., 1996; Jia et al., 2008; Kivelson et al., 2004; Volwerk et al., 1999). As a result, field lines become draped over the moon and Alfvén wings are formed at larger distances to Ganymede (Kivelson et al., 2002, 2004; Neubauer, 1980, 1998). These Alfvén wings connect to Jupiter's polar ionosphere, generating auroral footprints (Bonfond et al., 2013, 2017; Grodent et al., 2009; Hue et al., 2022). Ganymede's mini-magnetosphere can be divided into distinct regions of different field line geometries: "open" field lines emerge from the moon's high-latitude regions, connecting to Ganymede at one end and Jupiter at the other. The open field lines funnel energetic magnetospheric particles toward the moon's polar regions (e.g., Fatemi et al., 2016; Jia & Kivelson, 2021; Paty & Winglee, 2004). On the other hand, "closed" field lines emerge from low-latitude regions and connect to Ganymede at both ends (Jia & Kivelson, 2021). The boundary between these regions is referred to as the open-closed field line boundary (OCFB) and coincides with the locations of the moon's auroral ovals (e.g., Duling et al., 2022; Saur et al., 2015). Magnetic field lines at mid-to-high latitudes in Ganymede's tail region are open and allow particles to enter or escape the moon's magnetosphere (Frank et al., 1997; Williams, Mauk, & McEntire, 1997; Williams, Mauk, McEntire, Roelof, et al., 1997). In the upstream hemisphere, closed field lines generated by Ganymede's internal dipole extend about 30° north and south from the magnetic equator and up to $2 R_G$ from the surface (e.g., Jia et al., 2008; Kivelson et al., 1998; Williams, Mauk, & McEntire, 1997). The closed field lines in the downstream hemisphere span approximately half the latitude compared to the trailing hemisphere (e.g., Duling et al., 2014). Downstream, Ganymede's mini-magnetosphere extends up to $\sim 10 R_G$ along the flow direction (e.g., Jia & Kivelson, 2021; Kivelson et al., 2004).

Ganymede's internal dipole moment is tilted 176° from its spin axis and therefore its field is oriented nearly anti-parallel to the ambient Jovian field near the moon's equator (Kivelson et al., 2002). This configuration results in favorable conditions for magnetic reconnection (Jia & Kivelson, 2021; Kaweeyanun et al., 2020). Reconnection occurs at Ganymede's ramside magnetopause and in its magnetotail, and was identified as the primary mechanism for energy and plasma transfer from Jupiter's magnetosphere into Ganymede's local interaction region (Kaweeyanun et al., 2020). Observed surface brightness asymmetries between the (bright) leading and (dark) trailing hemispheres of Ganymede were suggested to be the result of reconnection in the magnetotail accelerating particles toward the moon's surface (e.g., Fatemi et al., 2016; Khurana et al., 2007). High flow shear along Ganymede's magnetopause flanks also supports the development of Kelvin-Helmholtz instabilities in these regions (Kaweeyanun et al., 2021; Masters, 2017).

Our knowledge of Ganymede's magnetic and plasma environment is largely based upon in situ measurements acquired by the Galileo spacecraft, which performed six close flybys of the moon between June 1996 and

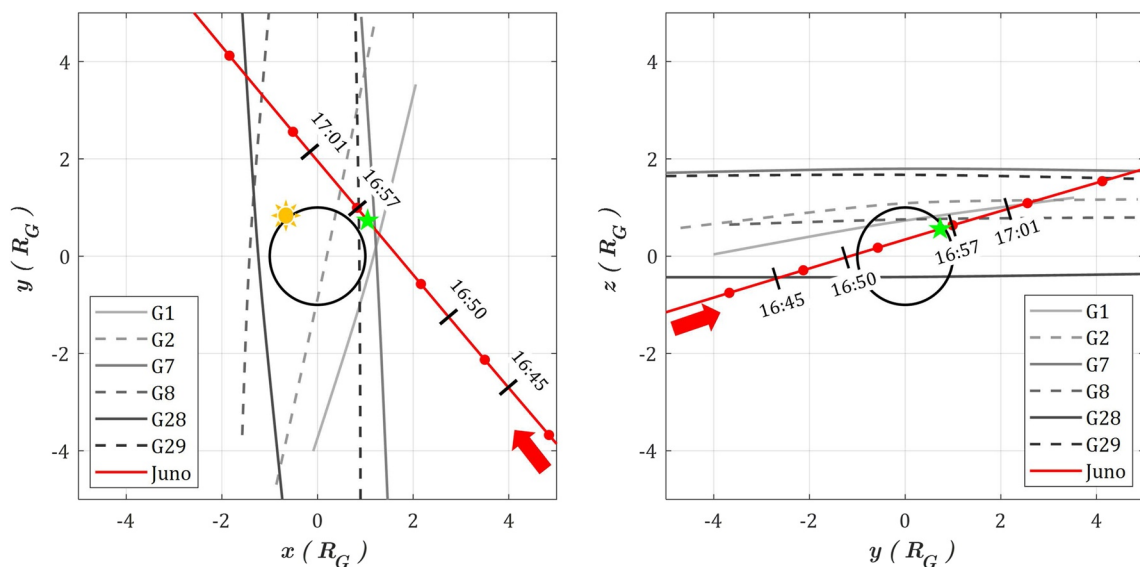


Figure 1. Trajectories of the six Galileo (gray lines) and one Juno (red line) close flybys of Ganymede in the (left) $z = 0$ and (right) $x = 0$ planes using the GPhiO Cartesian coordinate system (see text for definition). The small red circles along the Juno trajectory represent 5 min time intervals starting at 16:42:00 UTC. The green star designates the point of Juno's closest approach at an altitude of 1,046 km ($0.40 R_G$) at 16:56:08 UTC on 7 June 2021. The red arrows indicate the direction of motion of the Juno spacecraft, and Ganymede itself is represented by a circle of radius $1 R_G$. Transitions between regions of different plasma properties along the Juno trajectory (as described in Allegri et al. (2022)) are identified by black bars and labeled with the corresponding times in UTC. Details on these features are discussed in the text. The observed “wake” region identified in Juno data by Allegri et al. (2022) are entered at about 16:45 UTC and exited around 16:50 UTC. Juno's inbound and outbound crossings of Ganymede's magnetopause occurred at approximately 16:50 and 17:01 UTC, respectively. The marker at 16:57 UTC identifies the transition from nightside (before marker) to dayside (after marker) and the yellow sun in the $z = 0$ plane indicates the subsolar point during the Juno flyby.

December 2000, as well as remote observations by the HST. The six Galileo flybys are denoted by their respective orbits and referred to as G1, G2, G7, G8, G28, and G29. The trajectories of these flybys are pictured in Figure 1, which uses the Ganymede-centered Cartesian GPhiO coordinate system. In this system the positive x -axis points in the corotational flow direction, the positive z -axis points northward along the Jovian spin axis, and the y -axis completes the right-handed system with the positive pointing toward Jupiter. The distance from the origin of the GPhiO system is denoted by r . The components of the magnetic field \mathbf{B} in this system are referred to as (B_x, B_y, B_z) . Among the Galileo flybys G8 was the only one that occurred when Ganymede was located near the center of the Jovian magnetospheric plasma sheet (Jia & Kivelson, 2021). During this flyby, the Galileo spacecraft passed through Ganymede's upstream magnetopause at low latitude where it detected a significant increase to the B_z component generated by strong currents along the boundary layer, with B_z flipping sign from about -100 nT just outside the moon's magnetosphere to $+80$ nT within. Low frequency oscillations suggested to be Kelvin-Helmholtz surface waves were observed during the G8 flyby near both the inbound and outbound crossings of Ganymede's magnetopause (Kivelson et al., 1998).

The other five Galileo flybys occurred when the moon was well above (G1, G2, G29) or well below (G7, G28) the center of the Jovian plasma sheet. These encounters also saw sharp rotations of the magnetic field when entering and exiting Ganymede's magnetosphere. The G28 flyby passed through the upstream magnetopause at low latitude in the moon's southern hemisphere and detected field enhancements in B_z and B_x due to magnetopause currents and field line draping, respectively. However, the field line draping and compression of Ganymede's magnetosphere are both weak when the moon is located far from the center of the Jovian plasma sheet. As a result, the magnetic field observations from these five Galileo flybys can largely be explained by a superposition of Ganymede's internal dipole and the ambient Jovian field. Due to the strong plasma interaction at the time of G8, such an approach is not suitable for that flyby (e.g., Jia et al., 2008; Kivelson et al., 1998, 2004).

On 7 June 2021, about 14 hr before reaching its 34th perijove (PJ34), the Juno spacecraft performed the first and only targeted flyby of Ganymede since Galileo over 20 years prior. It reached a closest-approach altitude of 1,046 km ($0.40 R_G$) over the moon's leading hemisphere. The flyby occurred when the incoming solar radiation was directed along the unit vector $(0.67, -0.74, 0.00)$ in GPhiO coordinates, leaving the leading hemisphere mostly in shadow (Hansen et al., 2022) and the dawn terminator located 48° clockwise from the positive y axis

in the $z = 0$ plane (see Figure 1 for reference). As shown in Figure 1, Juno approached the moon's downstream hemisphere from the Jupiter-averted half space and traveled toward upstream and Jupiter. The spacecraft moved from $-z$ to $+z$ during the encounter and passed the moon's leading hemisphere at low-to-mid latitude. Juno approached Ganymede on the nightside and transitioned to the dayside just after closest approach (see Figure 1), subsequently exiting the moon's mini-magnetosphere. Similar to G8, the Juno flyby occurred when Ganymede was located in the high density environment near the center of the Jovian plasma sheet (e.g., Valek et al., 2022; Weber et al., 2022), marking the first flyby in the downstream region under these conditions.

Juno's magnetometer (Connerney, Adriani, et al., 2017; Connerney, Benn, et al., 2017) detected significant field perturbations upon entry into Ganymede's interaction region (16:45–16:50 UTC in Figure 1), as B_z increased from about -65 to 0 nT at 16:45 UTC and the field magnitude reached a minimum of just below 10 nT at 16:46 UTC. A non-zero field component normal to the magnetopause was observed during the outbound magnetopause crossing (17:01 UTC), providing evidence for reconnection occurring at this location during the flyby (Romanelli et al., 2022). Juno's Waves Instrument (Kurth et al., 2017) measured the electron density of Ganymede's magnetosphere, revealing distinct differences between the nightside and dayside hemispheres. The nightside electron density gradually increased from about $5 \times 10^6 \text{ m}^{-3}$ to $15 \times 10^6 \text{ m}^{-3}$ and then abruptly jumped to $30 \times 10^6 \text{ m}^{-3}$ when transitioning to the dayside at approximately 16:57 UTC (see Figure 1). The electron density then dropped to $5 \times 10^6 \text{ m}^{-3}$ as Juno exited Ganymede's magnetosphere (Kurth et al., 2022). A radio occultation experiment conducted during the ingress detected signatures of Ganymede's ionosphere, finding a peak electron density of $(2 \pm 0.5) \times 10^9 \text{ m}^{-3}$ near the surface (Buccino et al., 2022). This value is approximately half of the previously established upper limit from Galileo's radio occultation observations at Ganymede (Kliore, 1998).

Measurements from the Jovian Auroral Distributions Experiment (JADE, see McComas et al., 2017) characterized the cold (ionospheric) and thermal (ambient Jovian) electron and ion distributions during the flyby. JADE provided novel insights into the composition of the ion populations near Ganymede, since Galileo's Plasma Experiment could not infer the composition of outflowing ionospheric ions (e.g., Eviatar, Vasylunas, & Gurnett, 2001; Frank et al., 1997). Inside the moon's magnetosphere, JADE detected mainly slow, cold ions alongside precipitating protons moving along the magnetic field lines. These observations indicate that Juno intersected a region of open field lines, allowing for the exchange of plasma between Ganymede's magnetosphere and its environment (Allegrini et al., 2022). The population of cold ions in Ganymede's pick-up tail was observed to consist of O^+ , O_2^+ , H^+ , H_2^+ , and H_3^+ (Valek et al., 2022). Whereas the most abundant light ion species (H_2^+) was observed to be approximately symmetric in density and energy about the inbound and outbound legs of Juno's flyby, the observed O_2^+ ions achieved maximum density nearly 2 min after closest approach at 16:58 UTC (Valek et al., 2022). The "wake" region, indicated in Figure 1 from 16:45 to 16:50 UTC, was identified in Juno plasma observations (Allegrini et al., 2022) and is located downstream and outside of the Jupiter-averted flank of Ganymede's magnetopause. JADE detected ions with a mass-to-charge ratio of 3 within this region, which are assumed to be H_3^+ that either leaked out of Ganymede's magnetosphere or were created in the wake from H_2^+ reacting with atmospheric H_2 (Allegrini et al., 2022; Valek et al., 2022).

Various models have been applied to provide three-dimensional context for Galileo and Juno observations from the Ganymede flybys. The ion gyroradii in the ambient Jovian plasma near Ganymede are at most ~ 100 km (Kivelson et al., 2004). Therefore, this interaction scenario is in a regime where both fluid models and hybrid models (fluid electrons, kinetic ions) can accurately represent the plasma interaction. The first resistive MHD model of Ganymede's plasma interaction (Ip & Kopp, 2002) generated a preliminary description of the moon's magnetosphere and bolstered earlier postulations that field-aligned currents drive the observed ultraviolet auroral emissions (Eviatar, Strobel, et al., 2001; Feldman et al., 2000). Subsequently, a multi-fluid model was used to explore Ganymede's magnetospheric structure and ionospheric outflow (Paty & Wingling, 2004, 2006; Paty et al., 2008). It was found that the energy of ionospheric O^+ exiting Ganymede's magnetosphere along open field lines over the polar caps was largely below the detection threshold of Galileo's Plasma Experiment. The model thereby provided an explanation for the lack of O^+ outflow in observations from the polar G2 flyby (Frank et al., 1997; Paty et al., 2008). In combination with a brightness model of Ganymede's auroral emissions, Payan et al. (2015) applied a multi-fluid model to identify short-term (time scale of minutes) and long-term (time scale of hours) variability of the moon's auroral brightness and morphology. These variabilities were suggested to correspond to reconnection processes at Ganymede's magnetopause and the moon's periodically changing position relative to the center of the Jovian plasma sheet, respectively (Payan et al., 2015). Another multi-fluid model included higher-order velocity moments of Vlasov's equation (namely, the pressure tensor and the heat

flux tensor) in order to evaluate the role of electron physics in reconnection at Ganymede's magnetopause (Wang et al., 2018). It was shown that the anisotropies in electron pressure play an important role in shaping the electric field in the reconnection region.

The MHD model of Jia et al. (2008, 2009, 2010) added a model of the spatially non-uniform anomalous resistivity to Ganymede's interaction region (Jia et al., 2008, 2009, 2010). In this model, reconnection is triggered only in regions where the local current density exceeds a certain threshold. The authors demonstrated that reconnection at Ganymede's upstream magnetopause occurs in intermittent bursts on time scales of 10s of seconds, despite ambient conditions that vary on much larger time scales of several hours. The MHD model of Duling et al. (2014) incorporated realistic boundary conditions for the magnetospheric currents at the moon's insulating surface by requiring that the radial component of the electric current vanishes at the surface. This model quantified the impact of plasma interaction currents on the magnetic field near Ganymede's surface during the G8 flyby. It was found that the field magnitude in regions threaded by closed field lines is reduced by up to 120 nT compared to a mere superposition of Ganymede's internal field and Jupiter's magnetospheric field. In the polar regions, the field magnitude was comparably enhanced.

Dorelli et al. (2015) described Ganymede's magnetosphere within the framework of Hall MHD. Their model showed the appearance of large-scale flux transfer events in the moon's magnetopause and magnetotail, with the bulk flow directed away from Jupiter. These flows resulted in the formation of asymmetric Kelvin-Helmholtz waves along the magnetopause boundary, with the amplitudes being larger along the Jupiter-facing than the Jupiter-averaged magnetopause. Additionally, the strongest field-aligned currents in the Hall MHD model occurred near the OCFB, suggesting that the Hall effect may contribute to the observed locations of Ganymede's auroral ovals (Dorelli et al., 2015). Tóth et al. (2016) coupled a Hall MHD model to a particle-in-cell model, providing kinetic treatment of electrons and ions in regions close to Ganymede. The model revealed flux transfer events along the moon's magnetopause that possessed magnetic signatures consistent with those observed during the Galileo flybys. These flux transfer events occurred in similar regions and on similar time scales as the previously identified signatures of bursty reconnection along the magnetopause (Jia et al., 2010). Zhou et al. (2019) utilized a similar combination of MHD and particle-in-cell models to calculate the flux densities of ions and electrons accelerated by reconnection at Ganymede's magnetopause. This study suggested that precipitation of energetic electrons, accelerated within the upstream reconnection region, contributes up to half of the peak brightness of Ganymede's auroral emissions (Zhou et al., 2019).

Several authors used hybrid simulations in conjunction with a particle tracing model to calculate maps of the precipitating energetic ion fluxes onto Ganymede's surface (Fatemi et al., 2016; Poppe et al., 2018), finding strong correlation between the modeled influx patterns and observed surface brightness asymmetries (Khurana et al., 2007). These results suggest that non-uniform influx of energetic magnetospheric ions is the primary driver of the moon's surface brightness patterns (Fatemi et al., 2016). Based on a similar hybrid model, Fatemi et al. (2022) showed that the Hall effect dominates ion dynamics at Ganymede's magnetopause and that velocity distributions of ions in this region are highly anisotropic: the velocity component parallel to the background Jovian magnetospheric field was revealed to significantly exceed the perpendicular component. Liuzzo et al. (2020) used particle tracing in conjunction with field output from a hybrid model to study the spatial distribution of energetic electron flux onto Ganymede's surface. This study revealed that electrons contribute an order of magnitude more than ions to the charged particle number flux bombarding the moon's polar regions. These authors found their modeled electron influx patterns to be highly inhomogeneous, having locally reduced fluxes in the trailing hemisphere where the protection by the perturbed electromagnetic fields is strongest.

Recently, Duling et al. (2022) studied Ganymede's magnetosphere during Juno's PJ34 flyby using an MHD model. The poleward emission edges of the moon's auroral ovals, as observed by Juno during the PJ34 flyby (Greathouse et al., 2022), were found to deviate in latitude by less than 1° from the OCFB produced by this model on the downstream side. Thus, these results support the notion of the auroral emissions being generated near the OCFB (see also McGrath et al., 2013). The model results of Duling et al. (2022) also suggest that Juno's trajectory during the flyby did not intersect the region of closed field lines near Ganymede's wakeside surface. In order to evaluate the geometry of the closed field line region during the Juno flyby, Romanelli et al. (2022) modeled Ganymede's magnetosphere during the flyby using a hybrid approach. This hybrid model (Romanelli et al., 2022) suggests that the extension of the closed field line region toward downstream is larger than in the MHD results of Duling et al. (2022), and that the Juno spacecraft traversed this region for several minutes near closest approach.

None of the preceding modeling studies investigated the structure and dynamics of Ganymede's tail of ionospheric pick-up ions. Given the recent availability of Juno observations from Ganymede's mid-range tail region, there is strong motivation to understand how different ionospheric species populate this domain. In this study, we combine the AIKEF hybrid model (Müller et al., 2011) with Juno magnetic field and plasma observations from the Ganymede flyby (Allegrini et al., 2022; Valek et al., 2022) to provide three-dimensional context for these data sets. The AIKEF model includes a multi-species ionosphere around Ganymede and resolves the flow shear between different ionospheric and magnetospheric ion species. These features of the model may be necessary to explain plasma observations from the wake region and to search for Kelvin-Helmholtz instabilities along the magnetopause. We investigate how ionospheric models of increasing complexity populate the moon's tail region with pick-up ions and affect plasma and magnetic field signatures along Juno's trajectory. We also compare our results with data obtained from Juno's Jovian Auroral Distributions Experiment (JADE) and magnetometer (MAG) instruments. Additionally, we investigate the possible growth of Kelvin-Helmholtz instabilities in the vicinity of Juno's flyby trajectory as well as their influence on the observable plasma and magnetic signatures.

This paper is structured as follows: in Section 2, we briefly introduce the AIKEF hybrid model and provide an overview of the input parameters for the various simulation setups. Our model results and their comparison against Juno observations are presented in Section 3. Our investigation is concluded in Section 4 with a brief summary of our major findings. In Appendix A, we provide additional evidence for the validity of our model by comparing its output against magnetometer observations from all six Galileo flybys of Ganymede.

2. Model Description

2.1. Hybrid Simulation Model AIKEF

To model Ganymede's near-space environment during the Juno PJ34 flyby, we apply the established hybrid code AIKEF (Müller et al., 2011). The AIKEF model treats electrons as a massless, charge-neutralizing fluid and ions as individual macroparticles. This kinetic treatment of the ions allows for the inclusion of physical processes arising from ion gyration, such as the Hall effect (e.g., Dorelli et al., 2015) and non-Maxwellian velocity distributions near the moon (e.g., Fatemi et al., 2022). In the wake region identified in plasma data just outside of Ganymede's Jupiter-averted magnetopause (Allegrini et al. (2022) and Figure 1), Juno's magnetometer measured magnetic field magnitudes as low as ~ 10 nT over a region spanning 100s of km (e.g., Romanelli et al., 2022; Weber et al., 2022). In this environment, O_2^+ pick-up ions moving at speeds near the bulk velocity (120–160 km/s, see Kivelson et al., 2004) possess gyroradii of up to 4,700 km ($1.8 R_G$). Thus, capturing the behavior of pick-up ions in this region requires a kinetic treatment of their dynamics.

The AIKEF model has been applied to other Galilean satellites of Jupiter, namely Callisto (Liuzzo et al., 2015, 2016, 2017, 2018, 2019a, 2019b, 2022) and Europa (Addison et al., 2021, 2022, 2023; Arnold, Liuzzo, & Simon, 2020; Arnold, Simon, & Liuzzo, 2020; Arnold et al., 2019; Breer et al., 2019). This hybrid code was also used extensively to model the plasma environment of Saturn's moon Titan (e.g., Simon et al., 2007; Tippens et al., 2022) and the interaction between the solar wind and Mercury's magnetic field (e.g., Müller et al., 2012). In the preceding studies of plasma interaction at Ganymede's neighbors Europa and Callisto, AIKEF achieved excellent quantitative agreement with Galileo observations of the magnetic field and plasma density (e.g., Arnold et al., 2019; Liuzzo et al., 2016; Müller et al., 2011). Notably, the model reproduced transitions between regimes dominated by field line draping and Callisto's induced dipole field (Liuzzo et al., 2016), as well as a localized magnetic perturbation consistent with a water vapor plume at Europa (Arnold et al., 2019). These examples demonstrate that the AIKEF model can generate quantitatively accurate representations of moon-magnetosphere interactions in the Jovian system. We provide additional model validation in Appendix A, where AIKEF output is compared against magnetometer observations from all six Galileo flybys of Ganymede.

Our study consists of five different model setups, successively increasing in the complexity of the applied atmosphere and ionosphere models. This approach enables us to identify which model components play a critical role in shaping the magnetic and plasma signatures observed by Juno during the PJ34 flyby. In this section, we first review the magnetospheric upstream parameters common to all five setups (see Table 1). Next, we discuss the atmosphere and ionization parameters specific to each setup (see Table 2). In setup I, we study Ganymede without taking into account any atmosphere or ionosphere in order to establish a “baseline” for the associated plasma and field perturbations. Only the moon's internal magnetic field (including both permanent and induced dipole

Table 1
Simulation Parameters for the AIKEF Model (Common to All Five Setups)

Parameter	Symbol [unit]	Value	Source
Background magnetic field	\mathbf{B}_0 (nT)	(−15, 24, −75)	Duling et al. (2022)
Background field magnitude	B_0 (nT)	80.2	Duling et al. (2022)
Ganymede's magnetic moment (permanent)	\mathbf{M}_{dip} ($\times 10^{27}$ J/nT)	(−4.1, 9.0, −131.0)	Kivelson et al. (2002)
Ganymede's magnetic moment (induced)	\mathbf{M}_{ind} ($\times 10^{27}$ J/nT)	(1.2, −1.8, 0.0)	Kivelson et al. (2002)
Upstream plasma number density	n_0 (cm ^{−3})	10	Jia and Kivelson (2021)
Upstream plasma mean ion mass	m_0 (amu)	14	Jia and Kivelson (2021)
Upstream plasma bulk velocity	\mathbf{u}_0 (km/s)	(130, 0, 0)	Jia and Kivelson (2021)
Upstream plasma ion temperature	$k_B T_0$ [eV]	100	Jia and Kivelson (2021)
Upstream plasma electron temperature	$k_B T_e$ (eV)	100	Jia and Kivelson (2021)
Convective electric field ($\mathbf{E}_0 = -\mathbf{u}_0 \times \mathbf{B}_0$)	\mathbf{E}_0 (mV/m)	(0, −9.8, −3.1)	(Calculated)
Alfvén velocity ($V_{A,0} = \frac{B_0}{\sqrt{\mu_0 m_0 n_0}}$)	$V_{A,0}$ (km/s)	148	(Calculated)
Alfvén Mach number ($M_{A,0} = \frac{u_0}{V_{A,0}}$)	$M_{A,0}$	0.88	(Calculated)

terms) is included in this run. Setup II introduces a symmetric O₂ atmosphere exposed to uniform electron impact ionization. A symmetric H₂ atmosphere, again with a uniform electron impact ionization rate, is added for setup III. The objective of setups II and III is to study the outflow patterns of the dominant heavy (O₂⁺) and light (H₂⁺) ionospheric species, and to evaluate their impact on the magnetic field and plasma signatures near the moon. In

Table 2
Parameters of Ganymede's Atmosphere and Ionosphere in AIKEF

Parameter	Symbol (unit)	Model setup					Source
		(I)	(II)	(III)	(IV)	(V)	
O ₂ column density	N_{O_2} (cm ^{−2})	—	1.5×10^{15}	1.5×10^{15}	1.5×10^{15}	1.5×10^{15}	Carnielli et al. (2020)
O ₂ scale height	H_{O_2} (km)	—	250	250	250	250	Hall et al. (1998)
O ₂ surface number density	$n_{\text{O}_2,0}$ (cm ^{−3})	—	6.0×10^7	6.0×10^7	6.0×10^7	6.0×10^7	(Calculated)
O ₂ e-impact ionization rate	v_{e^-, O_2} (s ^{−1})	—	1.0×10^{-7}	1.0×10^{-7}	1.0×10^{-7}	1.0×10^{-7}	Carberry Mogan et al. (2023)
O ₂ photo-ionization rate ^a	v_{p, O_2} (s ^{−1})	—	—	—	3.0×10^{-8}	3.0×10^{-8}	Carberry Mogan et al. (2023)
H ₂ column density	N_{H_2} (cm ^{−2})	—	—	7.5×10^{14}	7.5×10^{14}	7.5×10^{14}	Marconi (2007)
H ₂ scale height	H_{H_2} (km)	—	—	1,000	1,000	1,000	Shematovich (2016)
H ₂ surface number density	$n_{\text{H}_2,0}$ (cm ^{−3})	—	—	7.5×10^6	7.5×10^6	7.5×10^6	(Calculated)
H ₂ e-impact ionization rate	v_{e^-, H_2} (s ^{−1})	—	—	6.0×10^{-8}	6.0×10^{-8}	6.0×10^{-8}	Carberry Mogan et al. (2023)
H ₂ photo-ionization rate ^a	v_{p, H_2} (s ^{−1})	—	—	—	3.1×10^{-9}	3.1×10^{-9}	Carberry Mogan et al. (2023)
H ₂ O column density ^b	$N_{\text{H}_2\text{O}}$ (cm ^{−2})	—	—	—	—	4.8×10^{15}	Leblanc et al. (2023)
H ₂ O scale height	$H_{\text{H}_2\text{O}}$ (km)	—	—	—	—	200	Vorburger et al. (2022)
H ₂ O surface number density ^b	$n_{\text{H}_2\text{O},0}$ (cm ^{−3})	—	—	—	—	2.2×10^8	(Calculated)
H ₂ O e-impact ionization rate	$v_{e^-, \text{H}_2\text{O}}$ (s ^{−1})	—	—	—	—	1.0×10^{-7}	Carberry Mogan et al. (2023)
H ₂ O photo-ionization rate ^a	$v_{p, \text{H}_2\text{O}}$ (s ^{−1})	—	—	—	—	2.1×10^{-8}	Carberry Mogan et al. (2023)

^aSunlit hemisphere only. ^bValue at subsolar point (see Figure 1).

setup IV, we add dayside photo-ionization for both atmospheric species (O_2 and H_2) in order to analyze the role of asymmetric ionosphere formation. Setup V adds an H_2O atmospheric “bulge” concentrated around the dayside apex, with uniform electron impact and photo-ionization rates included. This setup accommodates the latest HST observations, which identified a persistent, localized H_2O bulge in Ganymede’s neutral envelope (Leblanc et al., 2023; Roth et al., 2021). This setup also facilitates the analysis of ionospheric flow dynamics for pick-up ions with intermediate weight (between O_2^+ and H_2^+).

Additional information on the AIKEF model can be found in Müller et al. (2011). Previous studies using AIKEF (e.g., Feyerabend et al., 2015; Kriegel et al., 2011, 2014) provide detailed coverage of the techniques for implementing atmospheres and ionospheres in the model, so only a brief description is provided here.

2.2. Hybrid Simulation Setup

Our hybrid model uses the Ganymede-centered GPhiO Cartesian coordinate system (described in Section 1), with a simulation domain spanning $-12 R_G \leq x \leq 18 R_G$, $-15 R_G \leq y \leq 15 R_G$, and $-20 R_G \leq z \leq 20 R_G$. Whenever an ion hits the surface of the moon or one of the six outer boundaries of the AIKEF model domain, it is deleted from the simulation. We utilize AIKEF’s hierarchical grid refinement structure to generate three levels of resolution. The model setup consists of three nested cuboids, with Ganymede located near the center of the inner-most and highest resolution cuboid. When moving toward the moon, the grid cell size is reduced by a factor of two at each boundary between cuboids. From the innermost to outermost cuboid, the grid size and span of each refinement level are given by: $0.027 R_G$ for $-4 R_G \leq x \leq 6 R_G$, $|y|, |z| \leq 4 R_G$, then $0.054 R_G$ for $-6 R_G \leq x < -4 R_G$ and $6 R_G < x \leq 10 R_G$, $4 R_G < |y|, |z| \leq 8 R_G$, and then $0.114 R_G$ for $-12 R_G \leq x < -6 R_G$ and $10 R_G < x \leq 18 R_G$, $|y|, |z| > 8 R_G$. Ionospheric ions drift toward downstream ($+x$) in the direction of the ambient Jovian plasma flow. Therefore, the region of increased grid resolution is extended farther in the downstream direction than toward upstream. The simulation is run until the upstream Jovian plasma has completed at least one full passage through the entire AIKEF domain, by which point the field configuration in the vicinity of Ganymede has reached a quasi-stationary state.

A summary of the model parameters characterizing the upstream flow is provided in Table 1. AIKEF treats the Jovian background field near Ganymede \mathbf{B}_0 as spatially uniform. As shown by Duling et al. (2022), this background field vector around closest approach to Ganymede is given by $\mathbf{B}_0 = (-15, 24, -75)$ nT. The moon’s internal magnetic field is represented by the sum of the permanent dipole and induced magnetic moments, $\mathbf{M}_0 = \mathbf{M}_{\text{dip}} + \mathbf{M}_{\text{ind}}$ (see Table 1). Ganymede’s permanent magnetic dipole moment is set to the value of $\mathbf{M}_{\text{dip}} = (-4.1, 9.0, -131.0) \times 10^{27}$ J/nT, as obtained by Kivelson et al. (2002) and analogous to Duling et al. (2022). Recently, Weber et al. (2022) performed an analysis across magnetometer data from three Galileo flybys and the Juno flyby to calculate updated spherical harmonic coefficients for Ganymede’s intrinsic dipole moment. These authors arrived at a value of $\mathbf{M}_{\text{dip}} = (-4.9, 10.2, -130.9) \times 10^{27}$ J/nT, which is very close to our chosen value.

To represent the inductive response of Ganymede’s subsurface ocean (e.g., Saur et al., 2015), we adopt the expression for the induced dipole moment given by Kivelson et al. (2002),

$$\mathbf{M}_{\text{ind}} = -\frac{2\pi\alpha R_G^3}{\mu_0} (B_{0,x}, B_{0,y}, 0), \quad (1)$$

where $B_{0,x}$ and $B_{0,y}$ are the x and y components of the Jovian background field \mathbf{B}_0 . An “efficiency parameter” $\alpha = 0.84$ (Kivelson et al., 2002) is introduced to account for finite electrical conductivity of the ocean shell and a thickness well below $1 R_G$. As suggested by Kivelson et al. (2002), the phase lag of the induced field at Ganymede can be considered negligible. Thus, Equation 1 yields $\mathbf{M}_{\text{ind}} = (1.2, -1.8, 0.0) \times 10^{27}$ J/nT for the conditions of the Juno encounter. While the maximum surface magnitude of the induced field is small (~ 15 nT) compared to the peak surface magnitude of the permanent dipole field ($\sim 1,440$ nT), it still meaningfully contributes to the x and y components of the moon’s total magnetic moment \mathbf{M}_0 . In our model, Ganymede’s total magnetic moment is then given by $\mathbf{M}_0 = (-2.9, 7.2, -131.0) \times 10^{27}$ J/nT.

At Ganymede’s orbit, the impinging Jovian thermal plasma is composed of electrons, protons, and heavy ions like oxygen and sulfur (Bagenal et al., 2016; Kim et al., 2020; Kivelson et al., 2004). Consistent with preceding models (e.g., Duling et al., 2022; Fatemi et al., 2016, 2022; Jia et al., 2010; Romanelli et al., 2022), we use a singly charged ion species with mean mass $m_0 = 14$ amu to represent the thermal ion population incident upon the moon.

The ambient Jovian ion and electron temperatures in our model are set to $k_B T_0 = 100$ eV (Jia & Kivelson, 2021; Kivelson et al., 2004). The average number density n_0 of the ambient Jovian magnetospheric plasma at Ganymede's orbit varies from about $1\text{--}10 \text{ cm}^{-3}$ as a function of the moon's distance to the center of the Jovian plasma sheet, with the maximum value occurring at the center of the sheet (Bagenal & Delamere, 2011). Ganymede was located near the center of the Jovian plasma sheet during the Juno flyby (Hansen et al., 2022). We therefore use a number density of $n_0 = 10 \text{ cm}^{-3}$ for the incident plasma, which is in agreement with ion density measurements obtained by Juno's JADE instrument a few minutes prior to entering Ganymede's magnetosphere (Allegrini et al., 2022). Our choice of upstream density is also consistent with the electron densities of $5\text{--}12 \text{ cm}^{-3}$ measured by the Juno Waves instrument during PJ34, just outside of the moon's magnetosphere (Kurth et al., 2022).

Only the thermal component of the Jovian magnetospheric plasma is included in our model. Accounting for the energetic ion population (e.g., Clark et al., 2022) would require lowering the time step in AIKEF to below what is computationally feasible (e.g., Liuzzo et al., 2019a, 2019b). The energetic ions only account for a small portion of the current density (Kim et al., 2020; Mauk et al., 2004), and therefore they do not make a significant contribution to the plasma interaction. As shown by several preceding hybrid modeling studies, the inclusion of the energetic ions is *not* required to accurately reproduce spacecraft observations or global magnetospheric structures at Ganymede (e.g., Fatemi et al., 2016, 2022; Poppe et al., 2018; Romanelli et al., 2022).

Upstream of Ganymede, the Jovian thermal plasma travels with a bulk velocity \mathbf{u}_0 in the $(+x)$ direction. We choose a value of $|\mathbf{u}_0| = 130 \text{ km/s}$, which is within the range of sub-corotation velocities ($120\text{--}160 \text{ km/s}$) observed at Ganymede's orbit (e.g., Jia & Kivelson, 2021; Kivelson et al., 2004; Krupp et al., 2004; Williams, Mauk, & McEntire, 1997). Our choice of bulk velocity and upstream plasma density yields an Alfvénic Mach number of $M_{A,0} = 0.88$ (see Table 1), which is consistent with the literature (e.g., Jia & Kivelson, 2021) and close to the values used in prior models (e.g., Duling et al., 2022; Fatemi et al., 2022; Jia et al., 2008). Outside of Ganymede's magnetosphere, the chosen parameters yield a convective electric field $\mathbf{E}_0 = -\mathbf{u}_0 \times \mathbf{B}_0$ that points into the $y < 0$ half space and also has a weak southward component (see Table 1).

2.3. Atmosphere and Ionosphere Models

Table 2 provides an overview of the atmosphere and ionosphere parameters used in each of the five AIKEF model setups (denoted I, II, III, IV, and V). Each setup builds upon the previous one by adopting its parameters and including additional atmospheric species and/or ionization mechanisms. Setup I represents a “baseline” run and does not include any atmosphere or ionosphere at all. This baseline setup functions as a reference for Ganymede's plasma interaction region and will enable us to identify perturbations generated by the ionospheric species included in subsequent configurations. This setup is also similar to those employed by previous hybrid models (e.g., Fatemi et al., 2016, 2022; Poppe et al., 2018).

In setups II–IV, the neutral density of each species in Ganymede's atmosphere is described by a barometric law,

$$n_s(r) = n_{s,0} \exp\left(-\frac{h}{H_s}\right), \quad (2)$$

where $n_s(r)$ is the number density of neutral species s at altitude h above the moon's surface, $n_{s,0}$ is the number density at the surface, and H_s is the corresponding scale height. The number density $n_{s,0}$ of neutral species s at Ganymede's surface is related to the scale height H_s and column density N_s by $n_{s,0} = N_s/H_s$.

In setup II, we introduce O_2 as the only atmospheric species because several studies suggest it to be the most abundant molecule in Ganymede's atmosphere (e.g., Carnielli et al., 2020; Leblanc et al., 2017; Marconi, 2007; Plainaki et al., 2015). Studies of Ganymede's neutral O_2 envelope found an approximately radially symmetric distribution about the moon's surface (e.g., Leblanc et al., 2017), which is consistent with the spherical symmetry inherent in our model atmosphere (see Equation 2). The O_2 scale height in our model is set to $H_{\text{O}_2} = 250 \text{ km}$, which is inside the range of $100\text{--}1,000 \text{ km}$ proposed by Hall et al. (1998) and consistent with values used in previous modeling studies of Ganymede's plasma interaction (e.g., Duling et al., 2014, 2022). The O_2 atmosphere is contained within the AIKEF model's highest resolution cuboid (see Section 2.2), where the grid resolution accommodates 3.5 cells per scale height H_{O_2} . We assume an O_2 column density of $N_{\text{O}_2} = 1.5 \times 10^{15} \text{ cm}^{-2}$. This value is slightly above the upper limit of $1.0 \times 10^{15} \text{ cm}^{-2}$ placed by Hall et al. (1998) and slightly below the recent estimate of $2.5 \times 10^{15} \text{ cm}^{-2}$ by Carnielli et al. (2020). Leblanc et al. (2023) recently proposed an O_2 column

density of about $4.0 \times 10^{14} \text{ cm}^{-2}$, which is also within a factor of 4 to the value we assume. Our chosen column density yields a surface O₂ number density of $n_{\text{O}_2,0} = 6.0 \times 10^7 \text{ cm}^{-3}$. Ionization of Ganymede's neutral O₂ envelope is driven primarily by electron impact ionization, the rate of which is about 5 times greater than that of photo-ionization (Carberry Mogan et al., 2023; Carnielli et al., 2019). In setup II, we include *only* electron impact ionization and adopt a constant (i.e., spatially uniform) ionization rate of $v_{e,\text{O}_2} = 1.0 \times 10^{-7} \text{ s}^{-1}$, in agreement with Carberry Mogan et al. (2023).

In setup III, we include an additional atmospheric species, H₂, which is suggested by numerous studies to be the second most abundant constituent of Ganymede's atmosphere and dominates at altitudes above 200 km (e.g., Jia & Kivelson, 2021; Leblanc et al., 2023; Marconi, 2007; Turk et al., 2014). Since the peer-reviewed literature does not provide any estimates of the scale height of H₂ at Ganymede, we set the value to $H_{\text{H}_2} = 1000 \text{ km}$, which is about half the estimated scale height of *atomic* hydrogen (e.g., Shematovich, 2016; Turk et al., 2014). The column density of H₂ is set to one half the column density of O₂, yielding $N_{\text{H}_2} = 7.5 \times 10^{14} \text{ cm}^{-2}$. This choice of N_{H_2} is consistent with models of the moon's atmosphere (e.g., Leblanc et al., 2017; Marconi, 2007; Shematovich, 2016), which found $N_{\text{O}_2}/N_{\text{H}_2} \approx 2-3$ over most of Ganymede's surface. Our H₂ column density also agrees with the value of $6.1 \times 10^{14} \text{ cm}^{-2}$ recently proposed by Leblanc et al. (2023), who used new HST observations to constrain the densities of Ganymede's atmospheric species. Our choice of scale height and column density yield an H₂ surface number density of $n_{\text{H}_2,0} = 7.5 \times 10^6 \text{ cm}^{-3}$, nearly an order of magnitude lower than that of O₂. As with molecular oxygen, electron impact ionization is the primary ionization mechanism for H₂ at Ganymede and exceeds the photo-ionization rate by about a factor of 3 (Carberry Mogan et al., 2023). For setup III, we assume a uniform electron impact ionization rate of $v_{e,\text{H}_2} = 7.0 \times 10^{-8} \text{ s}^{-1}$, again adapted from Carberry Mogan et al. (2023). Analogous to setup II, this third model configuration does not take into account any contribution to Ganymede's ionosphere from photo-ionization.

In model setup IV, photo-ionization of O₂ and H₂ is added to the sunlit hemisphere of Ganymede (see Figure 1 and Table 2). The moon's atmosphere has a maximum optical depth of 0.03 (Carnielli et al., 2019), so the incoming solar radiation is not significantly attenuated even close to the surface. Therefore, uniform photo-ionization rates of $v_{p,\text{O}_2} = 3.0 \times 10^{-8} \text{ s}^{-1}$ and $v_{p,\text{H}_2} = 3.1 \times 10^{-9} \text{ s}^{-1}$ for O₂ and H₂, respectively, are included in our model (Carberry Mogan et al., 2023; Carnielli et al., 2019).

For setup V, the model is again augmented by including a third atmospheric species: an H₂O density bulge is added about the subsolar point, as recently detailed by Roth et al. (2021) and Leblanc et al. (2023). To account for the concentration of H₂O around Ganymede's dayside apex, we use a modified barometric law adopted from Cervantes and Saur (2022) and apply it to the moon's sunlit hemisphere only:

$$n_{\text{H}_2\text{O}}(h, \vartheta) = \begin{cases} n_{\text{H}_2\text{O},0} \cos^\gamma(\vartheta) \exp\left(-\frac{h}{H_{\text{H}_2\text{O}}}\right) & \text{for } 0^\circ \leq \vartheta \leq 90^\circ \\ 0 & \text{for } 90^\circ < \vartheta \leq 180^\circ \end{cases} \quad (3)$$

In this expression, ϑ represents the angle between the unit vectors pointing (1) from Ganymede's center to its subsolar point and (2) from the moon's center to a given point in its atmosphere. While Cervantes and Saur (2022) did not study Ganymede's atmosphere, these authors found that $\gamma = 6$ best represents the H₂O bulge observed by HST around Europa's subsolar point (Roth, 2021). Due to the similarity between the extent of the H₂O density bulges observed at Europa and Ganymede (Leblanc et al., 2023), we adopt $\gamma = 6$ from Cervantes and Saur (2022) for our Ganymede model. Leblanc et al. (2023) found peak H₂O column densities of about $6 \times 10^{15} \text{ cm}^{-2}$ near the subsolar point when Ganymede's trailing hemisphere was illuminated, and about $1 \times 10^{15} \text{ cm}^{-2}$ when the moon's leading hemisphere was illuminated. During the Juno flyby of Ganymede, nearly 75% of the trailing hemisphere was exposed to solar radiation (see Figure 1). Accordingly, we linearly interpolate the maximum H₂O column density between these two cases to obtain a column density at the subsolar point of $N_{\text{H}_2\text{O}} = 4.8 \times 10^{15} \text{ cm}^{-2}$ in our model. Near Ganymede's terminator plane (i.e., $\vartheta \approx 90^\circ$), Roth et al. (2021) and Leblanc et al. (2023) found H₂O column densities below $1.0 \times 10^{13} \text{ cm}^{-2}$. This value is negligible compared to the column densities of O₂ and H₂ at the terminator. Therefore, we set $n_{\text{H}_2\text{O}}$ to zero in the terminator plane and in Ganymede's nightside hemisphere (see Equation 3).

In this study, we assume a scale height of $H_{\text{H}_2\text{O}} = 200 \text{ km}$, which is slightly larger than the value of 50 km proposed by Vorburger et al. (2022). However, our choice of $H_{\text{H}_2\text{O}}$ allows the AIKEF simulation grid to fully resolve the

radial structure of the H₂O envelope, while the region populated by H₂O still maintains a small size relative to Ganymede and the scale of the moon's plasma interaction region. The implications of our choice of H_{H_2O} on the results will be addressed in Section 3.3. The maximum surface number density of H₂O at the dayside apex is then given by $n_{H_2O,0} = 2.4 \times 10^8 \text{ cm}^{-3}$, which is about a factor of 4 and 30 greater than the (uniform) surface densities of O₂ and H₂, respectively. We expose H₂O to a uniform electron impact ionization rate of $\nu_{e,H_2O} = 1.0 \times 10^{-7} \text{ s}^{-1}$ and a dayside photo-ionization rate of $\nu_{p,H_2O} = 2.1 \times 10^{-8} \text{ s}^{-1}$, again adapted from Carberry Mogan et al. (2023). Other neutral species (OH, O, and H) also inhabit Ganymede's atmosphere, but they possess negligible column densities compared to those of O₂, H₂, and H₂O (e.g., Leblanc et al., 2017; Marconi, 2007). Therefore, these additional species are not included in our model. The inclusion of H₂O in setup V ensures that the dynamics of ionospheric species across the entire range of ion gyroradii occurring at Ganymede are included in our model: from small (H₂⁺), to intermediate (H₂O⁺, but also representative of other water group species), to large (O₂⁺).

3. Model Results for Ganymede's Plasma Environment

3.1. Setup I: No Atmosphere or Ionosphere

In this section, we present the results from model setup I. The initial conditions for this setup include the Jovian magnetospheric background field and Ganymede's permanent and induced dipole moments, but no atmosphere or ionosphere around the moon. Figure 2 displays two-dimensional illustrations of the modeled magnetic field components (B_x, B_y, B_z), magnetic field magnitude $|\mathbf{B}|$, Jovian plasma number density n_p , and bulk velocity magnitude $|\mathbf{u}_p|$ for this setup. All quantities in panels (a)–(f) are shown in the $y = 0$ plane of the GPhiO system, containing the center of Ganymede, the upstream flow velocity \mathbf{u}_0 , and the north-south component of the background field \mathbf{B}_0 . Panels (g)–(i) display the magnetic field components in the $x = 0$ plane, which is perpendicular to the upstream flow velocity. Magnetic field lines are plotted in black and Ganymede is indicated by a white circle about the origin of each panel.

The modeled open and closed field line regions of Ganymede's magnetosphere are visible in the $y = 0$ plane (Figures 2a–2d) and the $x = 0$ plane (Figures 2g–2i). Field lines connected to Ganymede on both sides comprise the closed field line region, while field lines that connect to the moon on one side, but exit the AIKEF model domain on the other (i.e., connect to Jupiter), are “open.” Field lines that do not connect to Ganymede at all correspond to the background magnetospheric field outside of the moon's magnetosphere. In both the $y = 0$ and $x = 0$ planes (Figures 2a–2d and 2g–2i, respectively), the open field lines emanate at high latitude from the moon's polar caps and the closed field lines are confined to near-equatorial latitudes. As shown in Figures 2a–2d, our modeled closed field line region in the $y = 0$ plane extends upstream to about $x = -1.9 R_G$. The upstream extension of our modeled closed field line region is consistent with the results of Duling et al. (2022) and Romanelli et al. (2022), who both found this region to extend to about $x = -2.0 R_G$ during the Juno encounter (see Figure 1 in either study). The modeled closed field line region in Figures 2a–2d extends downstream to $x = +1.6 R_G$, which is approximately the same value as obtained by Duling et al. (2022). In contrast to this, Romanelli et al. (2022) suggest that the closed field line region reached farther downstream during the Juno flyby than in our model, extending slightly beyond $x = 2 R_G$.

Analogous to Saur et al. (2015), we determined the latitude of the OCFB on Ganymede's surface by tracing the magnetic field lines emanating from the surface at various latitudes of a given longitude, classifying each line as either open or closed. We find the OCFB to be located at surface latitudes of 48°N and 43°S in the upstream hemisphere of the $y = 0$ plane, and 22°N and 25°S in the downstream hemisphere (see Figures 2a–2d). Our modeled OCFB latitudes are within a few degrees of the locations seen in the MHD simulations of Duling et al. (2022), and also coincide with the latitudes where the intensity of oxygen aurora emissions peaked during the Juno flyby (Greathouse et al., 2022).

Alfvén wings form above Ganymede's northern and southern polar caps, encompassing the open field lines that exit the moon's surface at high latitudes (Figures 2a–2d and 2g–2i). As shown by Neubauer (1980), the northern (–) and southern (+) Alfvén wing characteristics are oriented along $\mathbf{u}_0 \pm \frac{\mathbf{B}_0}{\sqrt{\mu_0 n_p m_0}}$. The wings are therefore tilted toward downstream, with the B_x component reduced in the northern wing (green in Figures 2a and 2g) and increased in the southern wing (red in Figures 2a and 2g). Using Equation 1 from Simon et al. (2022) and the parameters from Table 1, we find that the Alfvén wings are tilted toward downstream with respect to \mathbf{B}_0 by 36.3° in the northern hemisphere and 46.2° in the southern hemisphere (see Figures 2a–2d). This slight difference

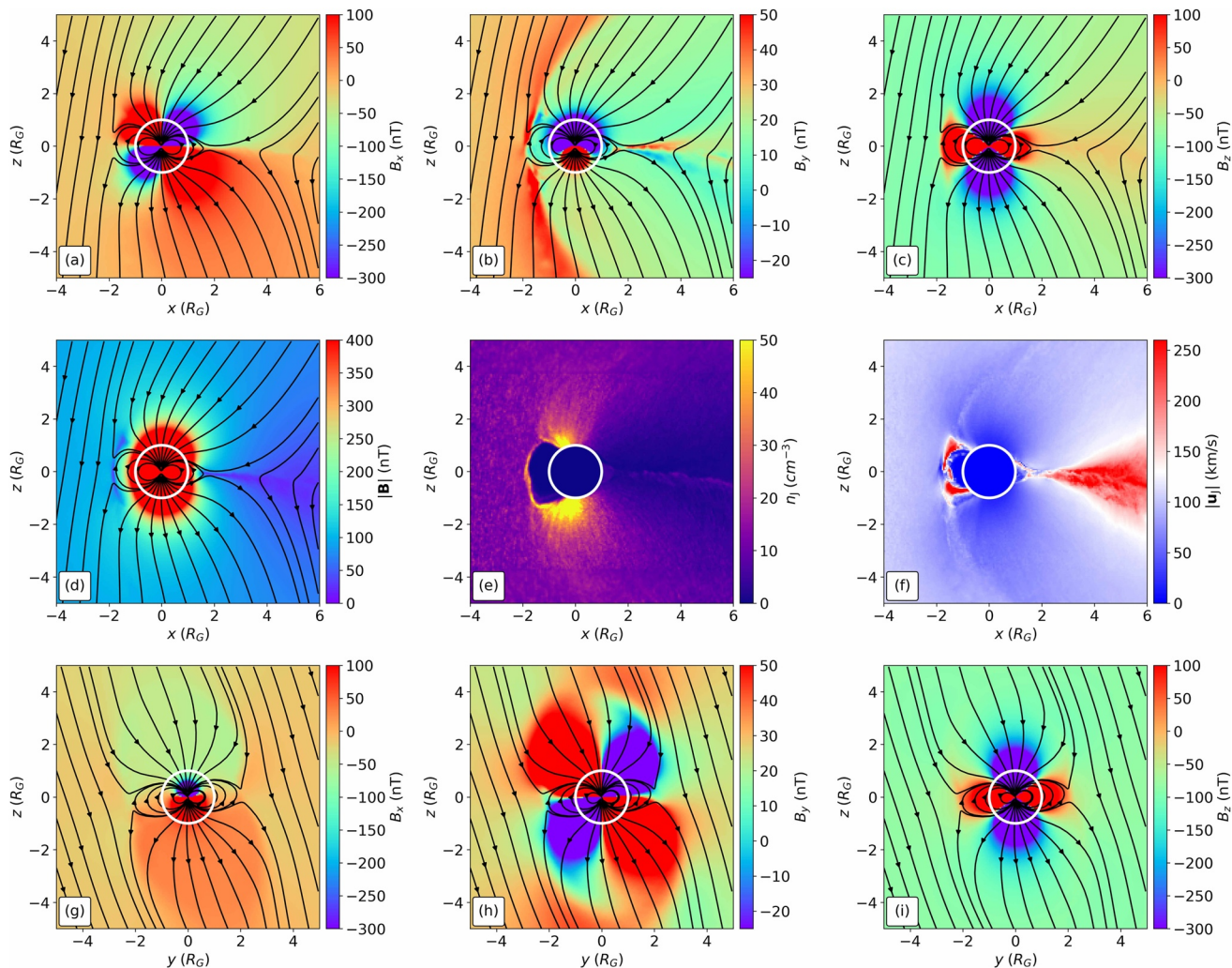


Figure 2. Two-dimensional color plots of AIKEF hybrid model results for setup I (no atmosphere or ionosphere; see Section 2.3 for details). For the $y = 0$ plane of the GPhIO coordinate system, the first two rows show: (a) B_x , (b) B_y , (c) B_z , (d) $|B|$, (e) the number density of the Jovian magnetospheric plasma n_j , and (f) the bulk velocity magnitude of the Jovian plasma $|u_B|$. Results for the $x = 0$ plane are displayed in the third row: (g) B_x , (h) B_y , and (i) B_z . In subplots (a)–(d) and (g)–(i), we also include a selection of magnetic field lines in black. Ganymede is denoted by the white circle of radius $1 R_G$ centered at the origin of each panel. To highlight the position of Ganymede's magnetopause, the B_y component in panels (b) and (h) utilizes different color scale limits than B_x and B_z .

between the tilts of the two wings is produced by the component of the background field antiparallel to the corotation direction, $B_{0,x} = -15$ nT. In the $x = 0$ plane, the Alfvén wing characteristics form an angle of 11.3° with the z axis, pointing away from Jupiter (−) in the north and toward Jupiter (+) in the south (see Figures 2g–2i).

The strong perturbations displayed near Ganymede in the B_x , B_y , and B_z components (Figures 2a–2d and 2g–2i) mainly stem from the superposition of the moon's internal dipole field with the Jovian magnetospheric background field. Ganymede's dipole field lines emanate outward from the southern polar cap ($z < 0$), turn northward and continue along loops of (approximately) constant latitude around the moon, and then return to Ganymede from above the northern polar cap ($z > 0$). As a result, the z component of the internal dipole field points southward (parallel to $B_{0,z}$) at high latitudes and northward (antiparallel to $B_{0,z}$) at low latitudes. Within the $x = 0$ and $y = 0$ planes, the superposition of Ganymede's internal dipole field and the primarily southward Jovian background field therefore produces two petal-shaped regions in B_z , where the moon's dipole amplifies the negative $B_{0,z}$ component of the background field (dark purple, see Figures 2c and 2i). Near the equatorial plane, the positive perturbation imposed by the dipole weakens $|B_{0,z}|$. In the vicinity of Ganymede's surface, the B_z component even flips sign to become positive (red, see again Figures 2c and 2i). Since Ganymede's magnetic moment points approximately southward, the B_z signatures generated near the moon by the superposition of the internal dipole

and the background field are nearly rotationally symmetric about the z axis. In three dimensions, B_z is therefore reduced within two bulb-shaped regions above the moon's polar caps (purple in Figures 2c and 2i), whereas the region of elevated B_z forms a torus along the moon's equator (red in Figures 2c and 2i).

In the $y = 0$ plane, Ganymede's internal dipole produces a shamrock-like pattern in the B_x component (purple and red in Figure 2a). As the moon's dipole field lines exit the southern polar cap, they bend toward upstream for $x < 0$ and toward downstream for $x > 0$. Superimposed with the (weak) negative $B_{0,x}$ component of the background field, this generates a region of negative B_x (purple) in the $(x < 0, z < 0)$ sector and a region of positive B_x (red) in the $(x > 0, z < 0)$ sector of the $y = 0$ plane (see Figure 2a). As the dipole field lines return to Ganymede in the northern hemisphere, they bend toward downstream for $x < 0$ and toward upstream for $x > 0$. This produces the regions of positive B_x (red) in the $(x < 0, z > 0)$ sector and negative B_x (purple) in the $(x > 0, z > 0)$ sector. The Alfvén wings, which show decreased B_x in the northern wing and increased B_x in the southern wing, slightly amplify the perturbations associated with the two "shamrock leaves" in the downstream hemisphere (Figure 2a).

The B_y component exhibits a similar, shamrock-like perturbation pattern in the $x = 0$ plane near the moon where the internal field is strong (red and purple in Figure 2h). Ganymede's dipole field curves away from the z axis for $z < 0$, corresponding to its bending toward Jupiter for $y > 0$ and away from Jupiter for $y < 0$. In the $(y < 0, z < 0)$ sector, this imposes a negative perturbation on the positive $B_{0,y}$ component of the background field, flipping the sign to negative (purple). Conversely, $B_{0,y}$ is amplified (red) by Ganymede's internal field in the $(y > 0, z < 0)$ sector (see Figure 2h). The reverse occurs in the northern hemisphere ($z > 0$) of the $x = 0$ plane, yielding positively (red, $y < 0$) and negatively (purple, $y > 0$) perturbed "shamrock leaves" in B_y .

The magnitude of the magnetic field $|\mathbf{B}|$, displayed in Figure 2d, is enhanced by at least a factor of five in an envelope around Ganymede, resulting from the dominance of the moon's intrinsic dipole in this region (red in Figure 2d). The field magnitude $|\mathbf{B}|$ becomes depleted in a broad region downstream of $x \approx 3 R_G$, decreasing to nearly an order of magnitude below the Jovian magnetospheric background field $|\mathbf{B}_0|$ (dark blue in Figure 2d). This results from the impinging Jovian field lines being diverted around Ganymede's mini-magnetosphere.

The location of Ganymede's upstream magnetopause is best visible in the B_y component: Figure 2b reveals a sharp boundary between the upstream region of slightly enhanced B_y (orange-red) and the downstream region of slightly depleted B_y (blue-green). In our model, the magnetopause possesses a stand-off distance from the ramside surface of approximately $0.9 R_G$ (measured along the negative x axis). Observations from the Juno flyby do not directly constrain the ramside stand-off distance of Ganymede's magnetopause, since the trajectory was mainly located in the downstream hemisphere (see Figure 1). However, the Galileo G8 flyby occurred under ambient conditions similar to those of the Juno flyby: Ganymede was positioned near the center of the Jovian magnetospheric plasma sheet and the upstream density was comparable to the value used in our model (e.g., Allegrini et al., 2022; Kivelson et al., 2004). During G8, Galileo crossed the upstream magnetopause at distances of $0.80 R_G$ (inbound) and $0.96 R_G$ (outbound) to Ganymede's surface. Both magnetopause crossings occurred at low latitudes and within 15° longitude of the upstream apex (Kivelson et al., 1998). The locations of the magnetopause crossings observed during G8 are in close agreement with our modeled ramside stand-off distance for the Juno flyby. On the Jupiter-facing and Jupiter-averted flanks, Ganymede's magnetopause coincides with the outer boundary of the open field line region (Figures 2g–2i). The magnetopause also confines the $\pm y$ extent of the shamrock-like perturbation pattern in B_y (Figure 2h), as well as the perturbations to B_x generated by draped Jovian field lines (Figure 2g).

Figure 2e displays the incident plasma being partially diverted around the upstream magnetopause and funneled toward Ganymede's surface just poleward of the closed field lines, populating two cusp-like regions (bright yellow in Figure 2e). These cusps correspond to densities of up to 5 times the upstream value. Our modeled density pattern demonstrates that most thermal ions impinging onto Ganymede's magnetosphere do not have sufficient energy to access the moon's surface at low latitudes, where it is "protected" by closed field lines (see also Cooper et al., 2001). Only a very small portion of the impinging ion population is able to penetrate the upstream magnetopause at low latitudes, with the number density dropping to below 1% of the upstream density above the moon's ramside apex (dark purple in Figure 2e). The inflow pattern of the Jovian thermal ions seen in Figure 2e is consistent with the findings of prior models (e.g., Fatemi et al., 2022; Poppe et al., 2018). The high-density cusps correspond to regions of low plasma velocity above Ganymede's poles (dark blue in Figure 2f): the velocity of the ions parallel (north) or antiparallel (south) to \mathbf{B} decreases when they travel along the "converging" field lines of the internal dipole. Downstream of Ganymede, the Jovian plasma density n_j is also

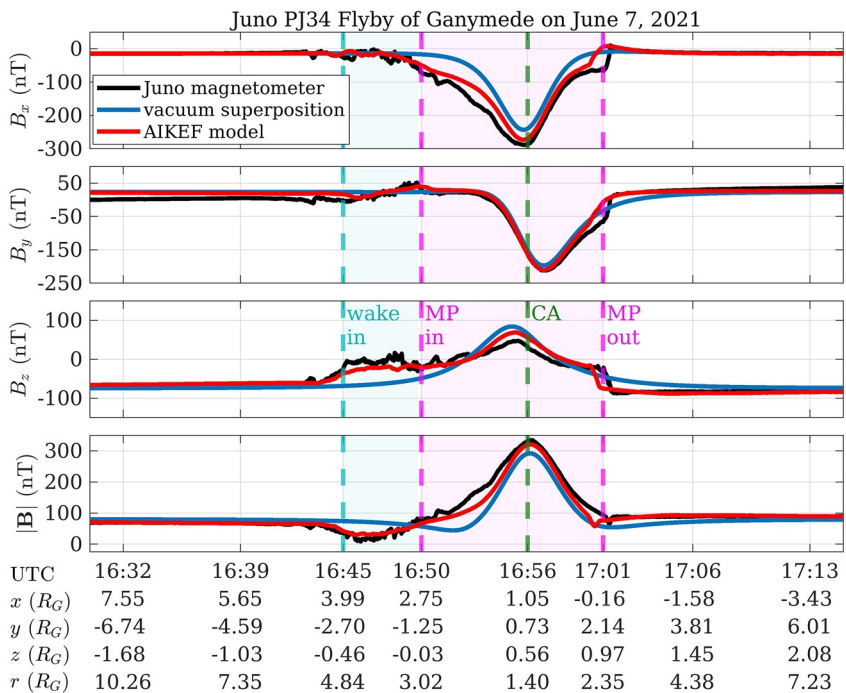


Figure 3. Observations and model results of the magnetic field components along Juno's PJ34 flyby trajectory of Ganymede. Included from top-to-bottom are B_x , B_y , B_z (given in GPhiO coordinates), and the field magnitude $|\mathbf{B}|$. Each panel displays the Juno magnetometer observations (black lines), hybrid model output (red lines), and the vacuum superposition model (blue lines), that is, a mere superposition of the Jovian magnetospheric background field and Ganymede's internal dipole field. The dashed teal line denotes Juno's entry into the “wake” region (Allegrini et al., 2022) at 16:45:08 UTC, while the dashed magenta lines denote the inbound (“MP in”) and outbound (“MP out”) magnetopause crossings at 16:49:48 and 17:00:39 UTC, respectively. These plasma regimes were identified by Allegrini et al. (2022) in data from the JADE instrument. The dashed green line (labeled “CA”) indicates Juno's closest approach to Ganymede at 16:56:08 UTC and corresponding to an altitude of 1,046 km (0.40 R_G). The light teal shading highlights the portion of Juno's trajectory located within the wake region, whereas the light magenta shading spans the segment of the trajectory inside Ganymede's magnetosphere. The location of Juno is provided below each timestamp along the bottom panel in GPhiO coordinates, with $r = \sqrt{x^2 + y^2 + z^2}$ denoting distance to the center of Ganymede.

depleted by a factor of about 10 (again depicted in dark purple). This reduction is generated by the diversion of the impinging flow around the moon's magnetosphere. The regions of high plasma velocity near the upstream magnetopause and in the downstream tail region (Figure 2f, red) are associated with local acceleration of the flow due to reconnection between antiparallel field lines from Jupiter and Ganymede (see also, e.g., Jia et al., 2009; Kaweeyanun et al., 2020; Romanelli et al., 2022).

Figure 3 displays time series of the magnetic field components B_x , B_y , and B_z , as well as the field magnitude $|\mathbf{B}|$, along Juno's trajectory during the PJ34 Ganymede flyby. Juno magnetometer observations are represented by the solid black lines. Results from the AIKEF hybrid model are plotted as red lines. The “vacuum superposition model,” which is the superposition of the undisturbed Jovian magnetospheric background field and Ganymede's internal dipole field, is plotted with blue lines. The vertical dashed lines indicate transitions between different sectors of Ganymede's interaction region, as identified in plasma observations from the JADE instrument (Allegrini et al., 2022). The observed magnetic field displays strong perturbations along the flyby trajectory in all three components, mainly from Ganymede's internal dipole, but also including contributions from plasma interaction currents. The deviation between the AIKEF model (red) and the vacuum superposition model (blue) at a given time indicates the modeled sign and magnitude of the contribution due to plasma currents.

We begin the discussion of Figure 3 by explaining the magnetic field signatures from the vacuum superposition model, which allows us to establish a “baseline” for the subsequent analysis of the time series from the AIKEF model and Juno. Ganymede's internal dipole dominates the magnetic signature observed along the segment of Juno's trajectory within the moon's magnetosphere (16:50 UTC to 17:01 UTC, shaded magenta in Figure 3). The

magnitude of Ganymede's dipole field scales as a function of r^{-3} , where r is the distance to Ganymede's center. Therefore, the vacuum superposition model (blue lines in Figure 3) displays maximum perturbations near closest approach at 16:56 UTC. Except for in the immediate vicinity of Ganymede's magnetopause, the trajectory inside the moon's magnetosphere was confined to the ($x > 0, z > 0$) sector and Juno remained at northern latitudes below 30°N (Hansen et al., 2022). Near the moon, the dipole field lines sampled by Juno thus pointed northward and were bent toward the z axis. Around closest approach, Juno also resided in the sub-Jovian hemisphere ($y > 0$), where Ganymede's dipole field lines bend away from Jupiter.

Therefore, the vacuum superposition model displays negative perturbations to both B_x and B_y near Ganymede, reaching minimums of -243 and -197 nT, respectively, within about 20 s of closest approach. Along the inbound segment of the trajectory within the Jupiter-averted ($y < 0$) hemisphere, Juno was too far downstream and too close to the $z = 0$ plane (see Figure 1) to sample a region of the dipole field with positive B_y . In B_z , the vacuum superposition model displays a positive perturbation near the moon: Ganymede's dipole field imposes a perturbation on the background field component $B_{0,z} < 0$, initially reducing $|B_z|$ and then flipping the sign of B_z to a maximum of about 85 nT just prior to closest approach (blue line in the third row of Figure 3). This corresponds to Juno traveling through the torus-shaped region of increased B_z (red) in Figures 2c and 2i.

Around Juno's entry into Ganymede's magnetosphere, the magnetic field magnitude of the vacuum superposition model dips below the Jovian magnetospheric background value. This corresponds to Juno's position between $x = 2 R_G$ and $x = 3 R_G$ downstream of Ganymede and close to the $z = 0$ plane, where the moon's dipole field points northward and depletes the predominantly southward background field \mathbf{B}_0 . As Juno approached Ganymede ($x \leq 2 R_G$), the perturbations in B_x and B_y (which increase the magnitudes of both components) map into the field magnitude of the vacuum superposition model and begin to dominate the behavior of $|\mathbf{B}|$. This causes the vacuum superposition model to display an enhancement in $|\mathbf{B}|$, reaching a maximum value of 292 nT near closest approach that is almost a factor of 4 above the background field strength $|\mathbf{B}_0| = 80$ nT.

We now discuss how the “vacuum” picture is affected by plasma interaction currents and how these currents generate the magnetic field signatures displayed by the AIKEF model and Juno observations. The “wake” region identified by Allegrini et al. (2022) resides just outside Ganymede's magnetosphere, downstream of the moon and along the Jupiter-averted magnetopause flank. We note that this region is distinct from Ganymede's “geometric” plasma wake, which is located directly downstream of Ganymede and defined by $x \geq 0$ and $\sqrt{y^2 + z^2} \leq R_G$. Juno observations within the wake indicate the presence of particles from both Ganymede's ionosphere and the Jovian plasma sheet (Allegrini et al., 2022, and Section 1).

As shown in Figure 3, Juno crossed through the wake region slightly south of the equator from about 16:45 UTC to 16:50 UTC. During this time, the observed B_x component decreases gradually from the background value $B_{0,x} = -15$ nT to about $B_x = -55$ nT (top panel in Figure 3). The B_x component of the vacuum superposition model remains nearly constant over the same time, indicating that the observed decrease in B_x is produced by plasma interaction currents. As shown in Figure 3, the AIKEF model generates a similar reduction of B_x throughout the wake region. Neither the modeled (red line) nor the observed B_x component (black line) contain a distinct jump corresponding to the inbound magnetopause crossing, but rather B_x progressively decreases until closest approach. Within Ganymede's magnetosphere, the dip in B_x from the internal dipole is amplified by field line draping in the northern Alfvén wing (which also reduces B_z ; green region in Figure 2g). In the time series from AIKEF, a minimum B_x value of -273 nT is reached near closest approach, which is slightly above the observed minimum of -288 nT. Within the moon's magnetosphere, our model setup I persistently underestimates the strength of the observed dip in the B_x component, deviating by as much as 40 nT from the values seen by Juno (near 16:53 UTC, red vs. black lines in the top panel of Figure 3). As we will show later, the inclusion of ionospheric pick-up ions in setups II–V results in the generation of stronger plasma currents near Ganymede, largely eliminating this deviation in B_x .

As indicated in Figure 3, Juno exited Ganymede's mini-magnetosphere around 17:01 UTC and very close to the $x = 0$ plane. The magnetic field components in this plane are also depicted in Figures 2g–2i. During the outbound magnetopause crossing, Juno observed a sharp increase in B_x of about 60 nT over a distance of $0.2 R_G$. This jump is associated with the spacecraft exiting the region of reduced B_x inside the northern Alfvén wing (green in Figure 2g). The AIKEF model displays a comparable jump in B_x at the outbound magnetopause crossing, both in magnitude and distance spanned. However, the modeled transition occurs about $0.2 R_G$ farther downstream and 1 min earlier than observed, which is similar to the model results of Duling et al. (2022). For setup I, a deviation

between modeled and observed magnetopause locations is indeed expected: due to the absence of Ganymede's ionosphere in the model, the counter pressure built up against the impinging Jovian flow is lower than in reality.

Similar to B_x , the observed B_y component in the wake region is not significantly affected by Ganymede's dipole (second panel in Figure 3). Instead, Juno observed a modest increase from the undisturbed (inbound) background field value of 5 nT to about 50 nT as a result of plasma interaction currents, shortly before exiting the wake at around 16:49 UTC. In the inbound segment of the trajectory, there is an offset of 19 nT between the background field in AIKEF ($B_{0,y} = 24$ nT, taken from Table 1) and the background B_y value of 5 nT observed by Juno. This stems from AIKEF using the average magnetospheric field at closest approach to determine \mathbf{B}_0 throughout the *entire* simulation domain. Whereas the B_y increase observed by Juno in the wake is about 45 nT, the enhancement displayed by AIKEF is a factor of 1.7 lower (about 26 nT). Inside Ganymede's magnetosphere, the moon's internal dipole dominates the B_y component. The B_y time series from the vacuum superposition model (blue), AIKEF model (red), and Juno observations (black) all largely overlap throughout the mini-magnetosphere until shortly before the outbound magnetopause crossing, indicating minimal perturbation to B_y from plasma currents inside of this region. During the outbound magnetopause crossing, the observed B_y component exhibits a similar jump as B_x , increasing by about 50 nT over a comparable distance of $0.2 R_G$ along the trajectory. Our model setup I does not reproduce the observed steepness of this transition and, similar to B_x , it again occurs about $0.2 R_G$ farther downstream than was measured by Juno.

The observed B_z component increases from the (inbound) background value of -60 nT at 16:43 UTC to about 0 nT at 16:45 UTC, immediately before Juno entered the wake region identified by Allegrini et al. (2022). The AIKEF model reproduces the steep inbound slope in B_z beginning near 16:43 UTC, but deviates from the observed B_z value at the inbound wake crossing (16:45 UTC) by about 20 nT. The observed positive B_z perturbation and slight deviation between AIKEF and the Juno data persist throughout the wake. The magnetic perturbations observed within the wake region will be revisited in Sections 3.2 and 3.3 when we include Ganymede's ionosphere: this region was found to be populated by pick-up ions (Allegrini et al., 2022) which may modify the plasma currents. However, we emphasize that even *without* the inclusion of Ganymede's ionosphere, the modeled B_z component does reveal perturbations in the wake region, and the B_z perturbations calculated by AIKEF are similar to those observed by Juno. Thus, the inclusion of Ganymede's ionosphere is not required to make the wake region "visible" in the magnetic field.

The observed contribution to B_z from plasma interaction currents flips sign (becoming negative) inbound of closest approach, indicated by the observed B_z time series (black) dropping below the vacuum superposition model (blue) in Figure 3. As a result, the maximum B_z value of 47 nT observed by Juno remains nearly 40 nT below the maximum value in the vacuum superposition model. In a similar way, AIKEF suggests the B_z signature from Ganymede's dipole to be weakened by the plasma interaction around closest approach. However, the effect is less pronounced than suggested by observations. Similar to the B_x and B_y components, the AIKEF model matches the sharpness and magnitude of the observed outbound magnetopause crossing in B_z , but the modeled magnetopause is again displaced about $0.2 R_G$ toward downstream.

The field magnitude $|\mathbf{B}|$ observed by Juno decreases in the wake region to its minimum value of around 10 nT. While in the wake, Juno traveled through the region downstream of Ganymede's magnetosphere where our model displays depleted $|\mathbf{B}|$, and which is also intersected by the $y = 0$ plane (dark blue in Figure 2d). The plasma interaction in the wake reduces $|B_z|$ (see third panel of Figure 3), which maps into the field magnitude in this region. As can be seen from the bottom panel of Figure 3, our model setup I quantitatively reproduces the reduction of $|\mathbf{B}|$ within the wake. This again supports the notion that an ionosphere around Ganymede is not required to generate discernible field perturbations within this region. Around closest approach, both the observed $|\mathbf{B}|$ and the field magnitude from AIKEF are dominated by Ganymede's internal dipole (blue vs. black and red lines in the bottom panel of Figure 3). A maximum value of $|\mathbf{B}| = 334$ nT is reached in Juno data just after closest approach, exceeding the peak value from the vacuum superposition model by about 40 nT. For both the AIKEF model and Juno observations, this overshoot of $|\mathbf{B}|$ above the vacuum superposition model is caused by the enhancement to $|B_x|$ from field line draping in the northern hemisphere (see Figures 2a and 2d).

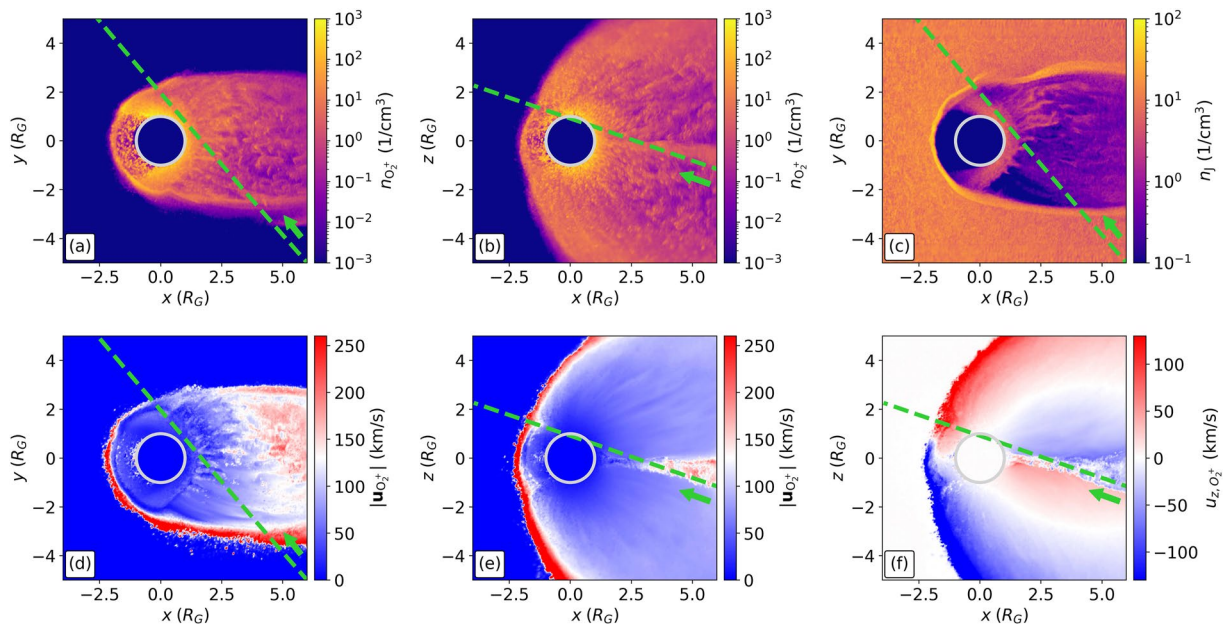


Figure 4. Two-dimensional color plots of the modeled Jovian plasma and ionospheric O_2^+ flow for setup II, which includes a symmetric O_2 atmosphere with uniform electron impact ionization (see Section 2.3). The figure includes: (a) ionospheric O_2^+ number density $n_{O_2^+}$ in the $z = 0$ plane, (b) $n_{O_2^+}$ in the $y = 0$ plane, (c) Jovian plasma number density n_j in the $z = 0$ plane, (d) ionospheric O_2^+ velocity magnitude $|u_{O_2^+}|$ in the $z = 0$ plane, (e) $|u_{O_2^+}|$ in the $y = 0$ plane, and (f) the z component of the ionospheric O_2^+ velocity u_{z,O_2^+} , again in the $z = 0$ plane. Regions with $u_{z,O_2^+} > 0$ are depicted in red, and regions where $u_{z,O_2^+} < 0$ are shown in blue. The projection of the Juno PJ34 flyby trajectory onto each plane is indicated by the dashed green line, with the arrow denoting the spacecraft's direction of travel. Ganymede corresponds to the light gray circle of radius $1 R_G$ centered at the origin.

3.2. Setup II: Radially Symmetric O_2 Atmosphere Around Ganymede

In this section, we present the model results for setup II. This configuration utilizes the same parameters for the upstream plasma and Ganymede's internal field as model setup I, but now includes a symmetric O_2 atmosphere exposed to a uniform electron impact ionization rate (see Section 2.3). Figure 4 displays two-dimensional color plots of the number densities (panels (a)–(c)) and bulk velocities (panels (d)–(f)) for both ion species involved in the interaction. The projection of Juno's trajectory onto each plane is indicated by the dashed green line. In Figure 5, we display the time series along the trajectory for the modeled ion number densities (Jovian and ionospheric) and the observed O_2^+ number density. Panel 5(a) includes Jovian plasma density profiles along the trajectory for both setup I (blue) and setup II (red). Panel 5(b) displays the O_2^+ number density observed by Juno (black, from Valek et al. (2022)) and calculated by AIKEF for model setup II (red). At the time of this writing, no time series data for the O_2^+ density collected outside of Ganymede's magnetosphere are available in the peer-reviewed literature. Additionally, there is no time series available for the Jovian magnetospheric plasma density within Ganymede's interaction region.

The Jovian plasma density n_j in Figure 4c is depleted by 1–2 orders of magnitude within Ganymede's magnetosphere near the $z = 0$ plane and in the tail region downstream of the moon (purple regions in Figure 4c). The impinging plasma is largely unable to penetrate into the moon's magnetosphere at low latitudes due to the presence of the closed field lines, accumulating instead outside of the magnetopause while flowing toward downstream (bright yellow-orange regions in Figure 4c). This enhancement in Jovian ion density occurs mainly near the ramside apex and along the Jupiter-facing flank ($y > 0$) of Ganymede's magnetopause. However, reconnection in the magnetotail occurring downstream at around $x \approx 2 R_G$ (see Figures 2a–2d) accelerates a portion of the Jovian magnetospheric plasma back toward the moon. This process produces a crescent-like feature in the Jovian ion density that wraps around Ganymede's downstream hemisphere, with values of n_j comparable to the upstream density n_0 (orange-purple crescent in Figure 4c). The hybrid model of Fatemi et al. (2022) shows a similar crescent pattern of enhanced Jovian ion density above the moon's downstream hemisphere; see Figure 2a in that work.

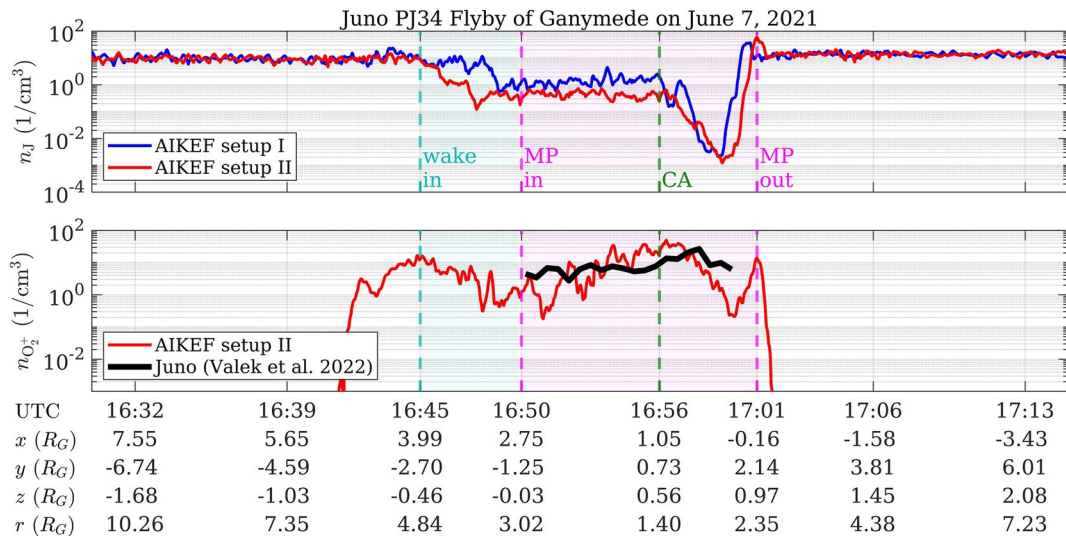


Figure 5. Juno observations and AIKEF model results of the number density of different plasma species along the PJ34 flyby trajectory of Ganymede. Panel (a) displays the number density of the Jovian plasma n_J calculated by AIKEF for both setup I (blue) and setup II (red). Panel (b) shows the O_2^+ number density $n_{\text{O}_2^+}$ observed by Juno's JADE instrument (black, provided in Valek et al. (2022)) and produced by the AIKEF model in setup II (red). The dashed vertical lines denote the same boundaries as in Figure 3, with the teal shading corresponding to the wake region and the magenta shading to Ganymede's magnetosphere, as identified in JADE data (Allegrini et al., 2022).

In setup II, the region downstream of Ganymede becomes populated with ionospheric O_2^+ particles, comprising a pick-up tail with sharp outer flanks (orange regions in Figures 4a and 4b). The upstream magnetopause position is visible in the oxygen ion density in both the $z = 0$ and $y = 0$ planes (orange and purple border). In the same way as the Jovian magnetospheric ions, a portion of the O_2^+ ions within Ganymede's magnetosphere are accelerated toward upstream by reconnection in the tail region. Similar to the Jovian plasma, this contributes to the formation of a crescent-like region of enhanced ionospheric O_2^+ density that wraps around Ganymede's downstream hemisphere in the $z = 0$ plane (bright yellow-orange in Figure 4a). The maximum number density within this O_2^+ population occurs near the surface of the moon and is on the order of $1,000 \text{ cm}^{-3}$. This value is only slightly lower than the maximum ionospheric electron density of $2,000 \text{ cm}^{-3}$ observed by Juno close to Ganymede's downstream surface (Buccino et al., 2022). The value from Buccino et al. (2022) is expected to exceed that in our model since Ganymede's actual ionosphere includes additional particle species that are not included in this AIKEF setup (Valek et al., 2022).

Some of the O_2^+ ions within the high-density crescent impinge onto the ramside magnetopause from the “inside.” In this region, the ionospheric O_2^+ is accelerated (red layer in Figure 4e) and diverted northward ($u_z > 0$, red in Figure 4f) in the $z > 0$ half space and southward ($u_z < 0$, blue in Figure 4f) for $z < 0$. Reconnection occurring downstream of the closed field line region ($x > 2 R_G$, see Figures 2a–2d) accelerates O_2^+ ions in that region toward downstream (red and white wedge-like region in Figure 4e). Immediately downstream of Ganymede, the high concentration of slow O_2^+ pick-up ions (blue in Figures 4d and 4e) reduces the convective electric field, thereby making the pick-up process less efficient. A similar “self-shielding” effect of a moon's tail against erosion due to pick-up has also been described extensively for, for example, Titan (Simon et al., 2007) and Callisto (Liuzzo et al., 2015).

The modeled O_2^+ velocity magnitude exhibits an asymmetry between the sub-Jovian and anti-Jovian flanks of Ganymede's pick-up tail (see Figure 4d): the anti-Jovian magnetopause flank ($y < 0$) reveals a layer up to $0.5 R_G$ thick of O_2^+ pick-up ions traveling at near twice the upstream bulk velocity ($2 |\mathbf{u}_0|$, thin red region in Figure 4d). Outside of the region of closed field lines, the O_2^+ pick-up ions gyrate largely perpendicular to the z axis and possess gyroradii of about $0.2 R_G$ (estimated using the upstream magnetic field and velocity from Table 1). The cycloidal trajectories of these ions have “bellies” that extend approximately $0.4 R_G$ away from Jupiter (see Equation 30 and Figure 2 of Simon et al., 2007). The Jovian plasma becomes accelerated along the outer flanks of Ganymede's magnetosphere, thereby locally enhancing the convective electric field in these regions. The

asymmetry in the cycloidal O_2^+ trajectories with respect to the direction of E_0 (pointing into the $y < 0$ half space, see Table 1) allows the O_2^+ ions to access this region of enhanced convective field along the anti-Jovian ($y < 0$) flank, but not along the sub-Jovian ($y > 0$) flank. This results in the elevated drift velocity of these ions toward downstream on the $y < 0$ flank of Ganymede's magnetosphere (red “ray” in Figure 4d). However, a similar feature is absent along the $y > 0$ flank. This idea is also supported by the time series of the modeled plasma density along Juno's trajectory (see Figure 5). The O_2^+ ions “leak” out of Ganymede's magnetosphere on the anti-Jovian flank of the pick-up tail, where they are intersected by Juno's trajectory starting at about 16:42 UTC (red line in Figure 5b). In this region, the O_2^+ population penetrates into the Jovian plasma outside Ganymede's magnetopause (red line in Figures 5a and 5b). Near the outbound magnetopause ($y > 0$), the O_2^+ population does not substantially extend outside of Ganymede's magnetosphere along the flyby trajectory (red line in Figure 5b). This is consistent with Juno observations, which revealed the presence of ionospheric ions within the wake region ($y < 0$), but not beyond the outbound magnetopause crossing (Allegrini et al., 2022).

Models of the plasma environments at Titan (e.g., Simon et al., 2007) and Callisto (e.g., Liuzzo et al., 2015) also display enhancements in the velocities of ionospheric pick-up ions along the planet-averted flanks of the moons' plasma tails. However, there is no magnetopause at either Titan or Callisto and therefore no boundary layer where the planetary magnetospheric plasma is prevented from substantially mixing with the ionospheric tail. The gyroradii of pick-up ions at Titan and Callisto are several times larger than the respective moon's radius (Liuzzo et al., 2015; Simon et al., 2007). As a result, the enhanced velocities of pick-up ions in the vicinities of Titan and Callisto are caused by the initial acceleration of these ions at the onset of their first “arc” of cycloidal motion. Thus, the mechanism generating the hemispheric asymmetries in pick-up ion velocities at Titan and Callisto is different from what we found at Ganymede (see Figure 4d).

Both the anti-Jovian (inbound) and sub-Jovian (outbound) flanks of the modeled pick-up tail possess steep density gradients along Juno's flyby trajectory: the modeled O_2^+ number density sharply increases from near-zero to 1 cm^{-3} at about 16:42 UTC over a length scale of about $0.3 R_G$, with a comparable rate of decrease occurring near the outbound magnetopause crossing (red in Figure 5b). After Juno entered the pick-up tail (around 16:43 UTC), the modeled O_2^+ density builds more slowly to a maximum of about 10 cm^{-3} (near 16:45 UTC), or very close to the undisturbed upstream density n_0 . This value is consistent with the maximum “heavy” ion density of 24 cm^{-3} (which includes all ion species but H^+) observed by Juno in the wake (Allegrini et al., 2022). Along Juno's trajectory, the modeled O_2^+ density within the pick-up tail then drops down to a minimum of just over 0.1 cm^{-3} at 16:48 UTC. Following this, the density slowly increases as the trajectory nears the Jupiter-averted magnetopause.

Within Ganymede's magnetosphere (magenta shading in Figure 5), the narrow range of ionospheric O_2^+ densities observed by Juno largely agrees with the AIKEF results for setup II (red vs. black lines in Figure 5b). Both the model results and the observed O_2^+ number density gradually increase inside the moon's magnetosphere from about 2 cm^{-3} (model) and 4 cm^{-3} (observations) to comparable maximums near closest approach: the modeled ionospheric O_2^+ population reaches a peak density of about 50 cm^{-3} just after 16:56 UTC, which agrees reasonably well with the observed maximum of 30 cm^{-3} . However, while the modeled peak in O_2^+ number density occurs about 30 s after closest approach, the observed peak in this value was detected by Juno 2 min after closest approach (see Figure 5b). The location and magnitude of the peak O_2^+ density in our model are also similar to those of the peak in electron density observed by the Waves instrument (Kurth et al., 2022, see their Figure 2). Shortly after the observed time series from Valek et al. (2022) ends (16:59 UTC), the modeled O_2^+ pick-up ion density briefly spikes to about 10 cm^{-3} . This feature reflects the accumulation of ionospheric ions inside of Ganymede's magnetopause (also visible in Figure 4a). The O_2^+ density largely disappears outbound of Ganymede's Jupiter-facing magnetopause, falling by over three orders of magnitude near the boundary layer (red lines in Figures 5a and 5b).

Both setup I and setup II display a reduced Jovian magnetospheric ion density within the wake region and an even stronger decrease inside of Ganymede's magnetosphere (see Figure 5a). However, while the upstream density in setup I (blue) does not significantly drop until after $1.0 R_G$ into the wake region (16:48 UTC), the density in setup II (red) begins to decrease as soon as the trajectory intersects the wake (16:45 UTC). In setup II, the Jovian ion density within the wake falls by over two orders of magnitude to a minimum of around 0.05 cm^{-3} at 16:48 UTC. This again contrasts with setup I, which displays a less pronounced minimum of about 1 cm^{-3} in the wake region, occurring much closer to the inbound magnetopause crossing at 16:50 UTC (blue in Figure 5a). The stronger

density decrease in setup II is caused by the ionospheric plasma pushing the Jovian plasma out of the region populated by O_2^+ ions through the pressure gradient forces at the steep outer flanks of the pick-up tail. Inside of Ganymede's magnetosphere, the Jovian ion density along the flyby trajectory remains a factor of 3–4 lower in setup II than in setup I. After closest approach, this value is further reduced to a minimum of about 10^{-3} cm^{-3} in both model setups. Following this drop, the Jovian ion density abruptly increases to near the background value at the outbound magnetopause crossing (about 17:00 UTC, see Figure 5a).

Figure 6a displays the magnetic field components observed along Juno's trajectory (black), the model results from setup II (red), and the output of the vacuum superposition model (blue). Figure 6b again features B_z , but zoomed in over the short segment of the trajectory centered around the observed outbound magnetopause crossing, and plotted versus r rather than time. The line labeled t_0 (light pink) corresponds to an arbitrary starting point in the time *after* the upstream flow has completed a full passage through the model domain and the large-scale features of the interaction (e.g., the OCFB) have reached a quasi-stationary state. The other lines represent “snapshots” of the modeled B_z component at times $t_0 < t_1 < t_2 \dots < t_5$, taken in increments of 54 s (starting at t_0). The increment between consecutive B_z snapshots corresponds to the time required by the Jovian plasma to travel about $2.7 R_G$, or about half the span of Ganymede's closed field line region along the x axis near the $z = 0$ plane. This “flip-book” reveals the time variability in the location of the outbound magnetopause along Juno's trajectory (see Figure 2a).

While the inclusion of the O_2^+ ionosphere produces quantitative changes to the modeled magnetic field signature near Ganymede, it has minimal *qualitative* impact on the moon's magnetic environment. When the O_2^+ ions are picked-up by the impinging Jovian magnetospheric plasma, they further decelerate the flow and bend the Jovian field lines, in addition to the bending caused by Ganymede's internal field (e.g., Neubauer, 1999). Along Juno's trajectory, this effect amplifies the reduction to B_x from field line draping seen in setup I: inside Ganymede's magnetosphere, the modeled B_x in setup II more closely matches the observed values and deviates from the minimum by only about 1 nT compared to 15 nT in setup I (Figure 3 and top panel in Figure 6a). The ionospheric O_2^+ also increases the effective size of the obstacle to the impinging flow. Within the wake region, the B_x component in setup II therefore drops slightly below the observed values. In contrast to this, the modeled and observed B_x signatures within the wake were almost indistinguishable in setup I.

The magnetic field perturbations near closest approach are dominated by B_x , which therefore also leaves the strongest imprint on the field magnitude $|\mathbf{B}|$ in the immediate vicinity of Ganymede. Within the moon's magnetosphere, the inbound and outbound flanks of the modeled $|\mathbf{B}|$ enhancement in setup II thus better match the observed values. The maximum of the modeled $|\mathbf{B}|$ in setup II falls within only ~ 1 nT of the observed maximum, with both of them occurring shortly after closest approach at about 16:56:30 UTC (Figure 6a). The modeled B_y component does not display meaningful differences between setups I and II: the time series from both AIKEF setups reveals minimal perturbations from plasma currents and largely overlaps with both the Juno observations and the vacuum superposition model. The B_z component in setup II exhibits slightly enhanced perturbations in the wake region by about 10 nT compared to setup I, approximately matching Juno observations as the spacecraft approached Ganymede's inbound magnetopause.

In model setup I, the outbound magnetopause crossing was located about $\Delta x = 0.2 R_G$ farther downstream and $\Delta r = -0.2 R_G$ closer to Ganymede than was observed by Juno (see Figure 3). However, in model setup II, increased counter-pressure from ionospheric O_2^+ inside of Ganymede's magnetosphere pushes the modeled magnetopause farther away from the moon. This causes the location of the modeled outbound magnetopause crossing to shift to a slightly later point in time (+1 min) and farther from the moon ($\Delta r \approx +0.2 R_G$) along the trajectory when compared to setup I. As can be seen from the modeled B_x and B_z components in Figure 6a, the modeled outbound magnetopause location demonstrates substantially better agreement with Juno observations in setup II. However, the presence of the O_2^+ ionosphere also introduces an additional *time variability* to the outbound magnetopause location and the corresponding jumps in the B_x and B_z components. As displayed in Figure 6b for the B_z component, the location of the modeled outbound magnetopause crossing varies by $\Delta r \approx \pm 0.15 R_G$ on time scales of about 1 min. Hence, the modeled location of the anti-Jovian magnetopause seen in Figure 6a merely represents a snapshot in time: the position of the modeled magnetopause crossing along Juno's trajectory continuously evolves as the incident plasma flows past the moon. The length scales of this variability are small compared to the overall size of Ganymede's magnetosphere. However, the uncertainty in the location of the *observed* outbound magnetopause crossing associated with this effect is significant: had Juno sampled the outbound magnetopause a minute earlier or later under identical ambient plasma conditions, our setup II results suggest that the crossing of

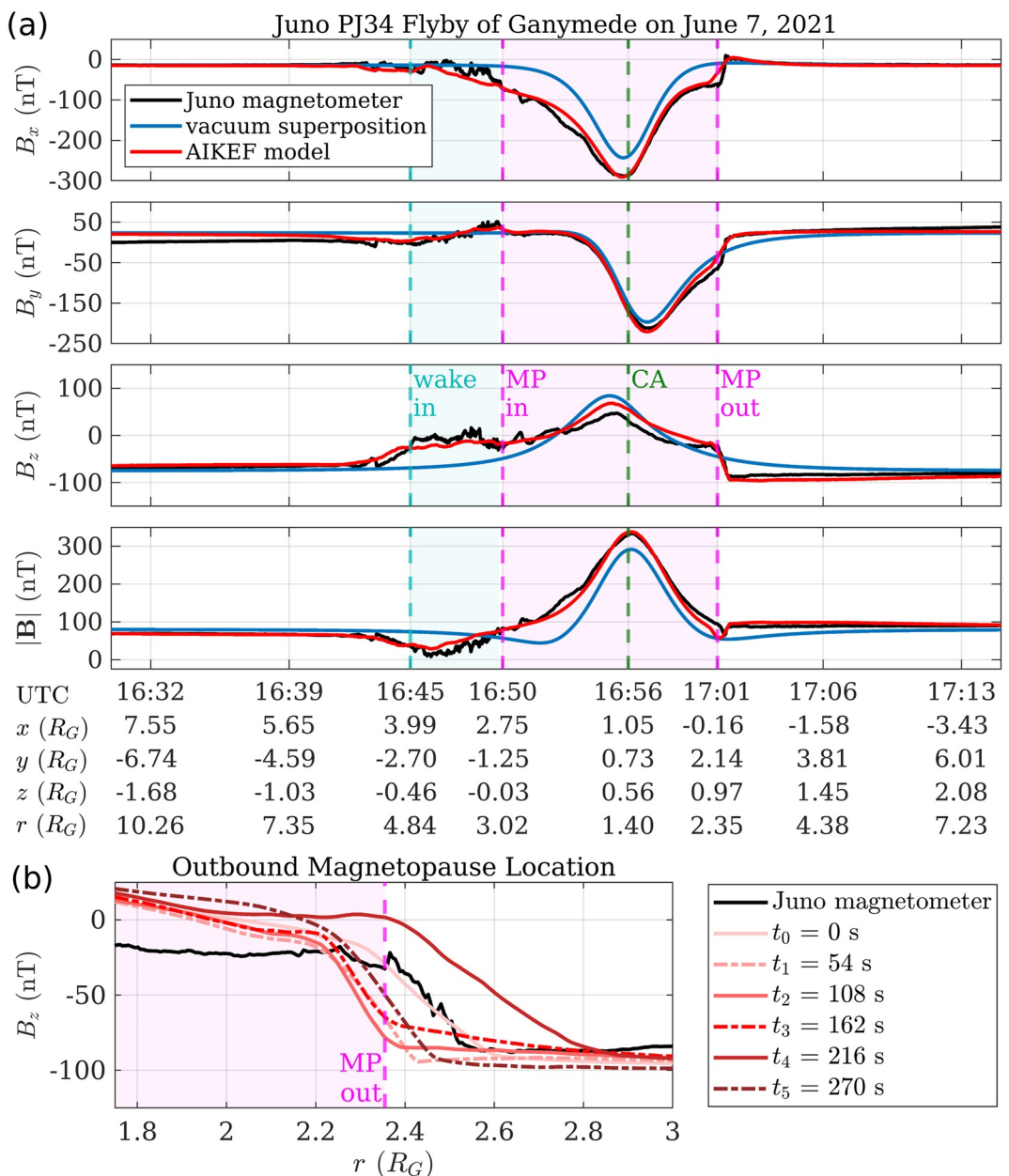


Figure 6. Comparison of modeled and observed magnetic field for setup II. Panel (a) displays time series of Juno magnetometer data, setup II results, and the output of the vacuum superposition model along the flyby trajectory. The layout is the same as in Figure 3, with B_x , B_y , B_z , and $|\mathbf{B}|$ arranged from top-to-bottom. The vertical dashed lines again indicate the boundaries between different sectors of Ganymede's interaction region. The teal and magenta shading correspond to the wake region and the moon's magnetosphere, respectively. Panel (b) displays the observed (black line) and modeled (colored lines) B_z component, zoomed-in about the observed outbound magnetopause crossing. All modeled results in panel (b) are obtained from setup II. The model result at time $t = t_0$ (light pink line) represents an arbitrary point in time *after* the large-scale features in the AIKEF model have reached a quasi-stationary state and the upstream plasma has completed at least one full crossing of the model domain. This time (t_0) also corresponds to the modeled magnetic field results in panel (a). The other colored lines represent the modeled B_z component at later points in time ($t_1 < t_2 \dots < t_5$), each of them separated by 54 s from the previous and the lines becoming increasingly darker as time progresses. This spacing corresponds to the time required for the upstream plasma to travel about $2.7 R_G$ in the $+x$ direction. The illustration in panel (b) indicates how the location of the modeled outbound magnetopause crossing along the flyby trajectory varies in time.

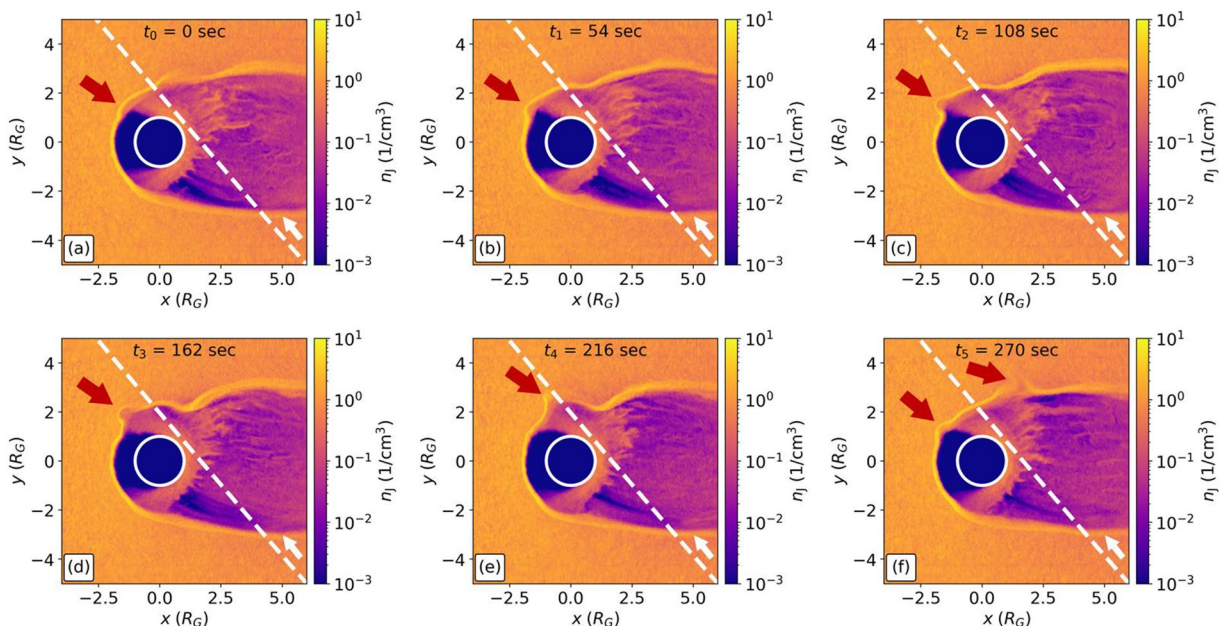


Figure 7. AIKEF results of the Kelvin-Helmholtz instability (KHI) as seen in the Jovian plasma density of setup II. All panels provide two-dimensional color plots of the Jovian ion number density n_i in the $z = 0$ plane. The red arrow in each panel identifies the KHI perturbation traveling along the sub-Jovian magnetopause flank, with the final panel including an additional arrow (on the left) to identify a second, subsequent KHI perturbation. Panel (a) corresponds to an arbitrarily chosen “start” time after the large-scale features in the model output have reached a quasi-stationary state. Each subsequent panel (b)–(f) advances the time by 54 s, with 270 s having elapsed in the final panel of the sequence (f). The points in time chosen to generate this illustration are the same as in Figure 6b. Juno’s flyby trajectory is indicated by the dashed white line and the accompanying white arrow corresponds to the spacecraft’s direction. Ganymede is identified by the white circle of radius $1 R_G$ centered on the origin.

this boundary layer would have been detected at a location up to $0.15 R_G$ closer to Ganymede or $0.15 R_G$ farther away from the moon.

The time-variability in the location of Ganymede’s Jupiter-facing magnetopause in setup II is caused by Kelvin-Helmholtz instability (KHI) propagating along this boundary. This instability forms as a result of shear flow between the dense O_2^+ populating Ganymede’s magnetosphere and the adjacent flow from Jupiter’s magnetosphere. We note that the KHI also manifests in setup I in the same region of the magnetopause (Jupiter-facing flank, $y > 0$). In that setup, it arises from velocity shear between the flow outside of Ganymede’s magnetopause and the Jovian magnetospheric plasma that populates the moon’s mini-magnetosphere and is accelerated toward upstream by reconnection in the tail region (see also Kaweeyanun et al., 2021). However, perturbations from the KHI in setup I are much weaker than in any of our four setups (II–V) which include an ionosphere, and the resulting spatial variability of the outbound magnetopause location along Juno’s trajectory is on the order of the grid resolution in AIKEF.

Figure 7 displays a “flip-book” of the time evolution of the KHI in setup II, providing two-dimensional context for the time variability of the sub-Jovian magnetopause location along Juno’s trajectory. Each panel shows a snapshot in time of the Jovian plasma density in the $z = 0$ plane. The points in time ($t = t_0, \dots, t_5$) sampled in Figure 7 are the same as indicated in Figure 6b. Ganymede’s magnetopause is located at the boundary between the low density (dark orange and purple) and background density (bright yellow-orange) regions in Figure 7, with the KHI appearing on the sub-Jovian ($y > 0$) flank of this boundary and indicated by the red arrows in each panel. The final panel (f) includes a second arrow (on the left) to indicate the beginning growth of a subsequent KHI perturbation.

In the snapshot at time $t = t_0$, a small wave-like perturbation starts to form in the $y > 0$ segment of the upstream magnetopause, as identified by the red arrow in Figure 7a. Subsequently, this perturbation grows in amplitude and is gradually accelerated along the Jupiter-facing magnetopause flank (Figures 7b and 7c). The KH wave then approaches Juno’s intersection with the sub-Jovian magnetopause flank, causing the location of the outbound magnetopause near the trajectory to be first pulled toward the moon by $\Delta r \approx -0.15$

R_G (Figures 7b–7d, see also times t_1 – t_3 in Figure 6b), and then pushed out by up to $\Delta r \approx 0.15 R_G$ (Figure 7e, see also time t_4 in Figure 6b). After this, the magnetopause retracts to just inside of the observed location again (Figure 7f, see also time t_5 in Figure 6b). The modeled KH waves propagate toward downstream at 30–50 km/s, or up to approximately one-third of the upstream plasma bulk velocity $|\mathbf{u}_0|$. Consecutive KHI bulges form at the Jupiter-facing ($y > 0$), upstream face of the magnetopause in time increments of just under 5 min: the next KH bulge can be seen forming at the same location as the first one at time t_5 (red arrow on left in Figure 7f).

The population of O_2^+ ions that “leak” out of the Jupiter-averted magnetopause flank (Figure 5, and hazy purple in Figure 4a) move toward downstream at velocities comparable to the bulk velocity $|\mathbf{u}_0|$ of the upstream plasma flowing around the magnetosphere (red in Figure 4d). This high O_2^+ velocity reduces the shear between Ganymede's ionospheric and Jupiter's magnetospheric flow, thereby suppressing the KHI formation along the Jupiter-averted magnetopause ($y < 0$). Due to the orientation of their cycloidal trajectories, O_2^+ pick-up ions remain inside of Ganymede's magnetosphere near the Jupiter-facing magnetopause flank (see Figures 4a and 4d). Therefore, the electromagnetic fields in the adjacent Jovian flow are unable to enhance the drift velocity of these ions, thereby generating a velocity gradient across the magnetopause that makes it susceptible to KHI growth. The asymmetric KHI formation in our model agrees with the analytical work of Kaweeyanun et al. (2021), who also suggested suppression of the KHI along the $y < 0$ magnetopause. However, the analytical calculations by these authors do not take into account any pick-up ions from Ganymede's ionosphere, and the asymmetry in KHI formation is explained solely through the opposite sense of ion gyration in Ganymede's equatorial magnetic field, compared to the sense in the ambient Jovian field (see Figure 4a of that work).

3.3. Setups III, IV, and V: Inclusion of H_2 and H_2O Atmospheres

In this section, we present the model results for setups III, IV, and V, each of which adds an additional element of complexity to Ganymede's atmosphere and/or ionosphere (see Table 2). These model configurations utilize the same parameters for the upstream plasma and Ganymede's internal field as setups I and II. In setup III, a symmetric H_2 atmosphere is included (in addition to the O_2 atmosphere), and Ganymede's neutral envelope is exposed to uniform electron impact ionization. Setup IV adds dayside photo-ionization to both O_2 and H_2 . Finally, setup V adds an atmospheric H_2O “bulge” centered about the subsolar point (see Section 2.3). This water component is again exposed to uniform electron impact ionization and dayside photo-ionization.

In Figure 8, we display two-dimensional color plots of the modeled ion density for all three ionospheric species (panels (a)–(g)), as well as the H_2^+ bulk velocity (panels (h)–(j)). The three columns correspond to setups III (left), IV (middle), and V (right). Figure 9 displays the time series along Juno's flyby trajectory for the observed and modeled number densities of O_2^+ (panel (a)) and H_2^+ (panel (b)). Again, time series of observed ion densities are available only for the segment of the trajectory inside of Ganymede's magnetosphere (16:50 UTC to 16:59 UTC, see Valek et al. (2022)). Across all setups, the modeled H_2^+ densities along the trajectory display excellent quantitative agreement with Juno observations from Valek et al. (2022); see Figure 9b. For O_2^+ , the inclusion of additional ionospheric components in setups III–V does not affect the agreement between the modeled and observed time series, compared to setup II (see Section 3.2 and Figure 9a).

The modeled ionospheric O_2^+ density patterns in the $z = 0$ plane are qualitatively similar across setups III–V (top row in Figure 8). Inside of Ganymede's magnetosphere and pick-up tail, the O_2^+ density in these setups show only minor quantitative differences from those in the output of setup II (see Figure 4a). The modeled O_2^+ density along the flyby trajectory confirms minimal qualitative differences between this quantity in setups II–V (see Figure 9a). Compared to model setup II, the O_2^+ pick-up tail in setups III–V (Figures 8a–8c) is slightly narrower perpendicular to the x direction at intermediate distances to Ganymede ($x \approx 1.5R_G$). This is also visible along Juno's trajectory in Figure 9a: the inbound segment of the flyby trajectory intersects the modeled O_2^+ population about $0.15 R_G$ farther outside the wake region in setup II (red) than in setups III–V (green, brown, purple).

Because the O_2^+ number density is comparable to that of H_2^+ throughout Ganymede's magnetosphere (see Figures 8a–8f, 9a, and 9b), the heavier O_2^+ ions drain a much greater amount of the momentum from the impinging Jovian flow. The H_2^+ mass density outside of the moon's magnetosphere (where no O_2^+ is present) is exceeded

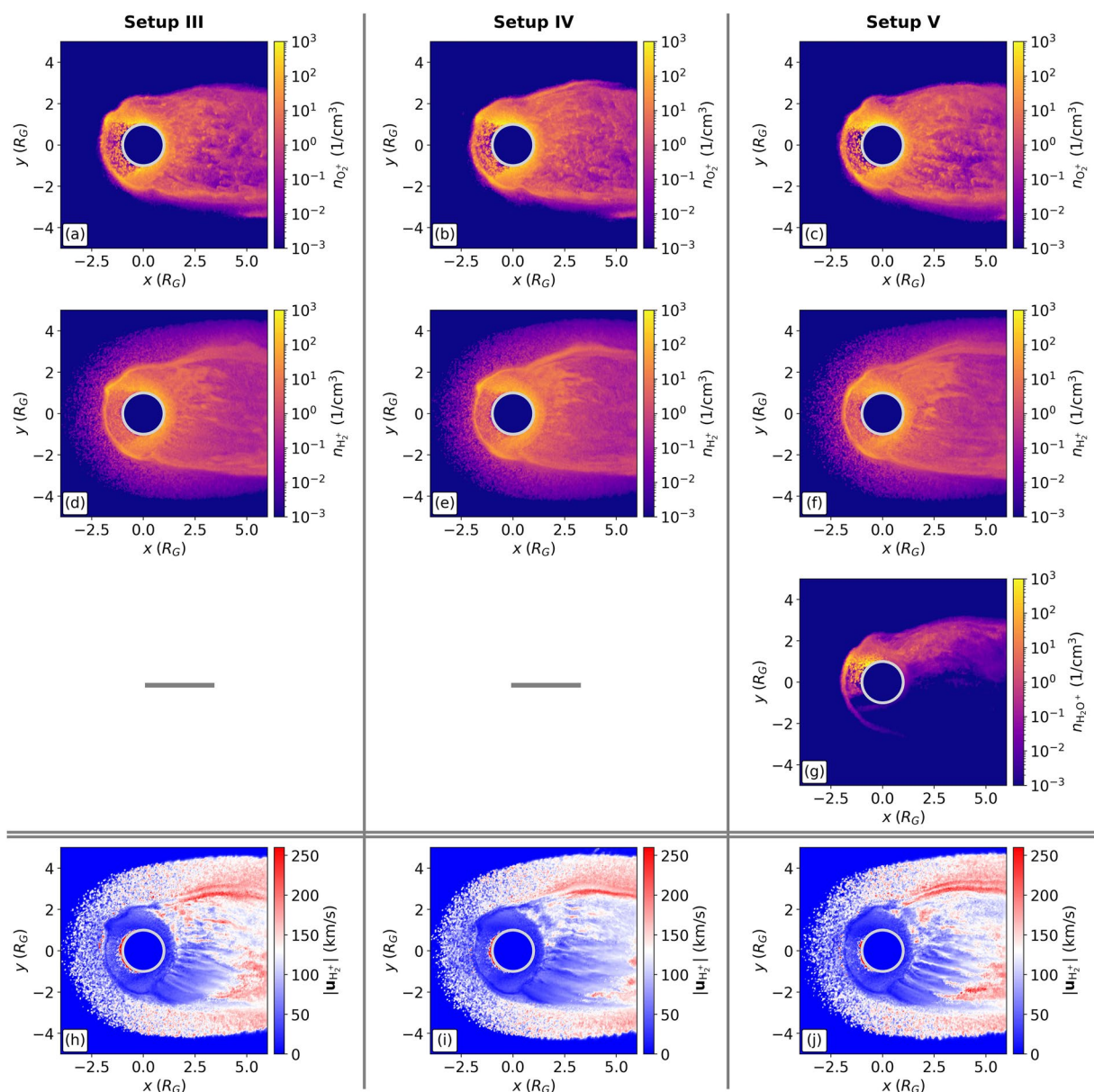


Figure 8. Two-dimensional color plots of the modeled ionospheric densities and H_2^+ bulk flow velocity for setups III, IV, and V (see Section 2.3). Setup III includes a symmetric O_2 and H_2 atmosphere and exposes both species to uniform electron impact ionization. Setup IV then adds dayside photo-ionization of both O_2 and H_2 . Finally, an H_2O atmospheric bulge centered about the subsolar point (see Figure 1) is added in setup V, with all three neutral species subjected to uniform electron impact ionization and dayside photo-ionization. The figure includes: (a)–(c) ionospheric O_2^+ number density $n_{\text{O}_2^+}$, (d)–(f) ionospheric H_2^+ number density $n_{\text{H}_2^+}$, (g) ionospheric H_2O^+ number density $n_{\text{H}_2\text{O}^+}$, and (h)–(j) the magnitude of the H_2^+ bulk velocity $|\mathbf{u}_{\text{H}_2^+}|$. All plots are in the $z = 0$ plane, with Ganymede indicated by the light gray circle of radius $1 R_G$ centered at the origin. The columns correspond to setups III (left), IV (middle), and V (right). Because setup V is the only one containing H_2O^+ ions, only a single panel is shown in the third row of the figure.

by that of the Jovian plasma by at least three orders of magnitude. Thus, mass loading of the Jovian plasma by H_2^+ ions outside of Ganymede's magnetosphere does not appreciably decelerate the flow. In consequence, the light H_2^+ ions included in setups III–V can be considered as test particles throughout Ganymede's interaction region, that is, they do not substantively affect the structure of the O_2^+ pick-up tail (see Figures 8a–8c). An analogous behavior was found for the light hydrogen ions populating Titan's interaction region (e.g., see Simon et al., 2007). In setups III–V, a crescent of elevated H_2^+ density forms around Ganymede's downstream hemisphere (yellow in Figures 8d–8f) and largely overlaps with the high-density crescent of O_2^+ ions (yellow in Figures 4a and 8a–8c).

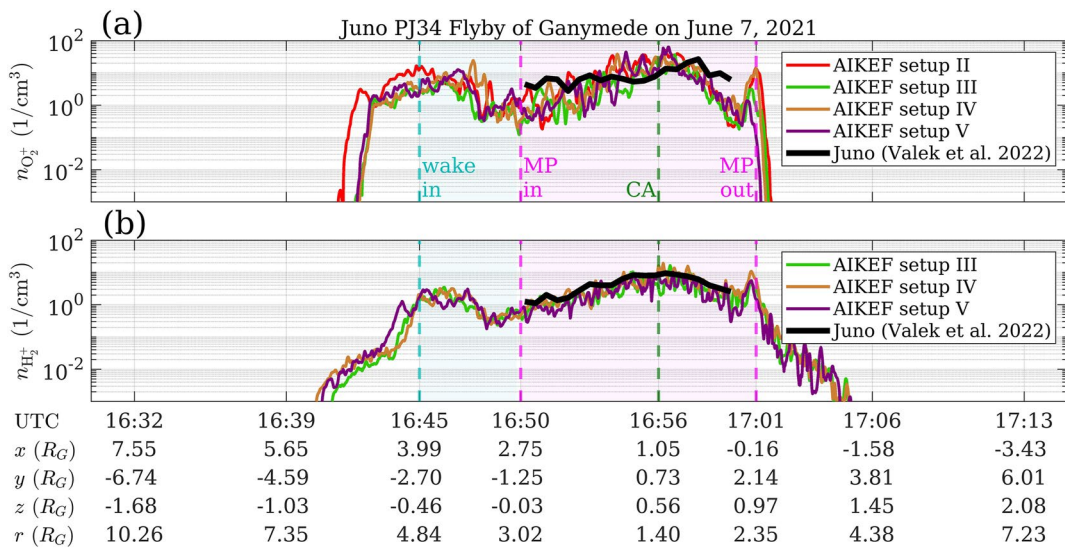


Figure 9. Juno observations and AIKEF model results for the number densities of ionospheric O_2^+ and H_2^+ ions along the PJ34 flyby trajectory. Panel (a) displays the number density of O_2^+ ions observed by Juno (black, provided in Valek et al. (2022)) and produced by the AIKEF model in setups II (red), III (green), IV (brown), and V (purple). The O_2^+ densities from setup II are the same as in Figure 5b, but we show them again here to facilitate comparison to the more complex ionosphere models. Panel (b) displays the H_2^+ number density observed by Juno (black) and produced by AIKEF for setups III (green), IV (brown), and V (purple). Since the hydrogen component of Ganymede's atmosphere is not included in setup II, the figure does not include a modeled time series of $n_{H_2^+}$ from setup II. The dashed vertical lines denote the same plasma boundaries as in Figures 3, 5, and 6. Teal shading indicates the segment of the trajectory inside of the wake region and magenta shading indicates the portion of the trajectory within Ganymede's magnetosphere, according to Juno JADE data (Allegrini et al., 2022).

The H_2^+ crescent extends to the upstream magnetopause in both hemispheres. As displayed by the O_2^+ and H_2^+ densities in Figures 8a–8f, there are again KH waves visible on the Jupiter-facing magnetopause flank in setups III–V. The amplitudes and propagation velocities of these waves are similar to those produced in setup II (see Figure 7).

The atmospheric scale height of H_2 ($0.38 R_G$ in our model, see Section 2.3) is four times greater than that of O_2 and only about a factor of two smaller than the ramside stand-off distance of Ganymede's magnetopause ($0.9 R_G$, see Figures 2b and 4). As a result, a dilute envelope of H_2 surrounds Ganymede's magnetosphere. The associated H_2^+ ions form a symmetric “corona” outside of the magnetopause (hazy purple in Figures 8d–8f). Along the Juno trajectory, the region populated by H_2^+ is more extended (by about $0.6 R_G$ inbound and $1.3 R_G$ outbound) than the O_2^+ tail (Figures 9a and 9b). Consistent with these modeling results, Juno detected the presence of H_2^+ ions just prior to entering and after exiting Ganymede's magnetosphere. These detections occurred before (inbound) and after (outbound) O_2^+ was encountered along the trajectory (Allegrini et al., 2022). The H_2^+ ions produced outside of the moon's magnetosphere are picked up and carried toward downstream along the outer flanks of the magnetopause at speeds near the upstream bulk velocity $|u_0|$ (white and red in Figures 8h–8j). The inclusion of photo-ionization (setup IV) and the additional H_2O^+ component (setup V) have minimal quantitative impact on the bulk velocity of H_2^+ in Ganymede's interaction region.

Our model results show that the H_2^+ ions populate the wake region along the Jupiter-averted magnetopause flank at densities of up to about $0.5 n_0$ (Figures 8d–8f and 9b). Just outside the Jupiter-averted edge of the wake, the H_2^+ density falls sharply to below $10^{-3} n_0$ in all setups (16:44 UTC–16:45 UTC in Figure 9b). In contrast to this, the modeled O_2^+ in Ganymede's Jupiter-averted hemisphere maintains densities of about n_0 (between 16:42 UTC and 16:45 UTC in Figure 9a). The observed time series and model results for setups III–V all reveal a maximum H_2^+ density along the trajectory of about 10 cm^{-3} ($\approx n_0$), occurring near closest approach. After the observed time series ends, the H_2^+ population displays a similar behavior as O_2^+ : a local minimum in H_2^+ density occurs at 17:00 UTC, followed by an enhancement just before the outbound magnetopause crossing (Figure 9b).

A comparison of the ion number densities between setups III and IV (Figures 8a and 8d versus Figures 8b and 8e) illustrates that the inclusion of dayside photo-ionization has only very minor quantitative impact on the tail structure of the O_2^+ and H_2^+ ions. The modeled ion densities along Juno's trajectory in Figures 9a and 9b also indicate no discernible difference between setups III (green) and IV (brown) due to photo-ionization. This similarity stems from the small ratios of photo-ionization to electron impact ionization rates at Ganymede, which are about 0.3 for O_2^+ and 0.05 for H_2^+ (see Table 2). In model setup V, production of H_2O^+ ions is confined to the low-latitude region around the subsolar point in the Jupiter-facing, upstream hemisphere (see Figure 1). The H_2O component of Ganymede's atmosphere has a scale height of only $0.08 R_G$ (see Section 2.3). Therefore, most H_2O^+ ions are generated inside the closed field line region, which near the $z = 0$ plane extends from Ganymede's surface about $0.9 R_G$ toward upstream and $1.0 R_G$ into the Jupiter-facing and Jupiter-averted half spaces (see Figures 2a–2c and 2g–2i). As a result, the bulk of the newly generated H_2O^+ ions are unable to "break free" of the closed magnetic field lines and do not contribute to the formation of the moon's pick-up tail.

The dilute H_2O^+ pick-up tail that is still formed resides in the $y > 0$ half space due to the location of the subsolar point in the Jupiter-facing hemisphere during PJ34 (Figures 1 and 8g). The H_2O^+ tail displays peak densities of only about 0.5 cm^{-3} . Although H_2O possesses a similar neutral column density and production rate to O_2 , this is over an order of magnitude lower than for O_2^+ in the same region. The low density of H_2O^+ pick-up ions in Ganymede's tail agrees with observations, which place an upper limit of less than a few percent on the contribution of H_2O^+ to the total ion mass density detected by Juno's JADE instrument (Valek et al., 2022). In reality, the H_2O bulge about the subsolar point is suggested to have a smaller scale height (about 50 km, see e.g., Vorburger et al., 2022) than assumed by our model. Production of H_2O^+ would therefore be even more confined (in the radial direction), compared to the radial extension of the closed field line region. As a result, an even larger fraction of the H_2O^+ ions would remain "trapped" near Ganymede, and the H_2O^+ number density in the pick-up tail would be even lower than shown in Figure 8g. The confinement of escaping ions of a certain species to a narrow outflow channel has been observed by the Cassini spacecraft during its wakeside T9, T63, and T75 flybys of Titan (Coates et al., 2012; Szego et al., 2007). However, at Titan, such channels were populated only by ions of a single mass-to-charge ratio. In contrast to this, our results for Ganymede suggest that the tail "ray" formed by the H_2O^+ ions still overlaps with the much broader tails formed by O_2^+ and H_2^+ ions.

In setups III–V, the O_2^+ ions dominate the ionospheric outflow, with approximately 10^{27} ions per second (53 kg/s) exiting the model domain at its downstream face. The modeled pick-up rates of the two minor species, H_2^+ and H_2O^+ , are about 10^{26} and 10^{24} ions per second, respectively, corresponding to 0.3 and 0.03 kg/s . Paty et al. (2008) constrained ionospheric outflow at Ganymede using a multi-fluid model that included an ionosphere composed of the atomic O^+ and H^+ ions (compared to our choice of molecular ionospheric constituents). These authors estimated a total loss rate (for both ionospheric species combined) of 10^{26} ions per second. Hence, their value is about an order of magnitude lower than suggested by our model. This discrepancy may result from these authors' choice of 125 km for the scale height of both ionospheric species, which corresponds to approximately 0.5 and 0.125 of the atmospheric scale heights used in our model for O_2^+ and H_2^+ , respectively. A smaller scale height causes a greater proportion of ion production to take place inside of Ganymede's closed field line region, thereby reducing the fraction of ionospheric particles able to escape toward downstream.

Figure 10 displays the magnetic field components observed along Juno's trajectory (black) and the model results from setups II (red), III (green), IV (brown), and V (purple). Increasing the complexity of Ganymede's atmosphere and ionosphere (setups III–V) does not produce any substantial differences in the modeled magnetic field signature compared to setup II, which considers only ionospheric O_2^+ ions. In general, the four model setups which include an ionosphere around Ganymede can quantitatively reproduce all key features of the Juno magnetometer observations. This suggests that for wakeside flybys at intermediate distance, the observable magnetic signature is largely determined by the interaction between Ganymede's internal dipole and the impinging Jovian magnetospheric plasma (see setup I). However, the addition of an O_2^+ ionosphere slightly inflates the moon's magnetosphere, thereby improving agreement between the modeled and observed magnetic field. Adding the light H_2^+ ions (which behave like test particles) or the highly localized H_2O^+ bulge does not have a discernible impact on the modeled magnetic field downstream of Ganymede. Hence, the magnetic field signature observed during the Juno flyby is not suitable to indirectly "measure" the complexity of Ganymede's ionosphere. Such an attempt would have been feasible only if ion cyclotron waves had been detected during the encounter (at the gyrofrequencies of the respective ion species). However, such waves may only reach detectable amplitudes much farther downstream.

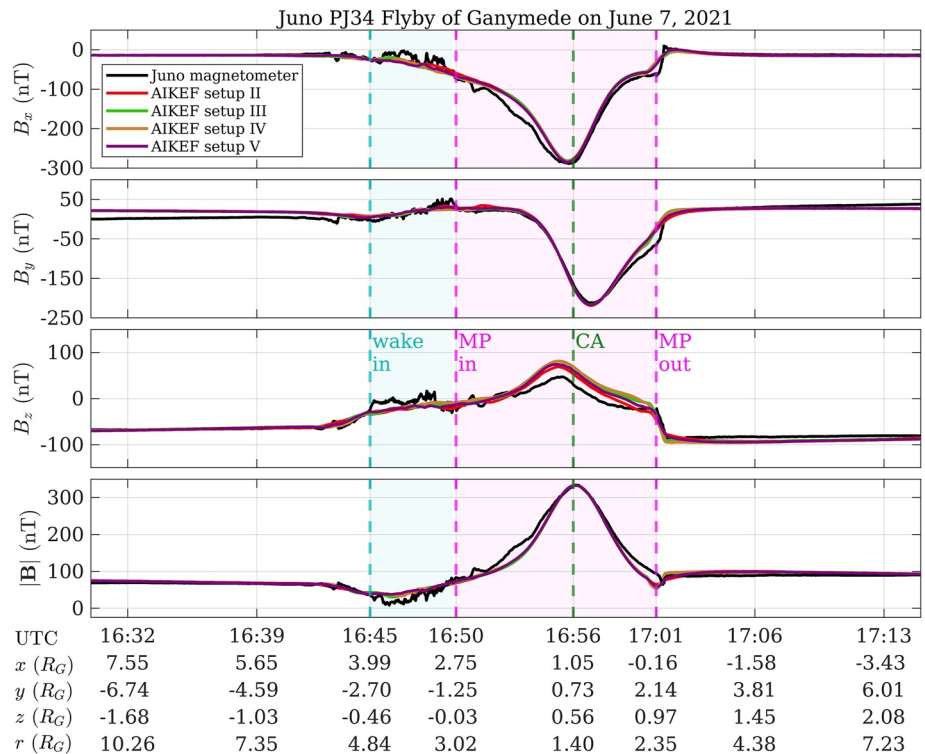


Figure 10. Comparison of the magnetic field components observed by Juno (black) and the AIKEF results for model setups II (red), III (green), IV (brown), and V (purple) along the PJ34 flyby trajectory. The layout is the same as in Figure 3, with B_x , B_y , B_z , and $|\mathbf{B}|$ arranged from top-to-bottom. The vertical dashed lines and background shading again correspond to boundaries between different regimes of Ganymede's interaction region. Results from setup II are shown here again to facilitate comparison with output from the configurations using more complex ionosphere models.

4. Conclusion

In this study, we have analyzed Ganymede's magnetic and plasma environment during Juno's PJ34 flyby on 7 June 2021. To accomplish this, we employed the AIKEF hybrid (kinetic ions, fluid electrons) plasma model (Müller et al., 2011), using upstream conditions consistent with those observed during the Juno flyby (e.g., Allegrini et al., 2022; Hansen et al., 2022; Kurth et al., 2022; Weber et al., 2022). Five ionosphere models of increasing complexity were evaluated, starting from a “baseline” case with no ionosphere at all (setup I). We then introduced a symmetric O₂ atmosphere around Ganymede (setup II), followed by symmetric O₂ and H₂ atmospheres within the same model run (setup III). In these two setups, uniform electron impact ionization was applied to Ganymede's neutral envelope. Dayside photo-ionization of both O₂ and H₂ was then added in setup IV. Finally, an atmospheric H₂O bulge centered about the subsolar point (e.g., Leblanc et al., 2023) was added, and all three constituents were exposed to both uniform electron impact ionization and dayside photo-ionization (setup V). We analyzed how the varying ionosphere configurations affect the magnetic field perturbations in Ganymede's interaction region. We also studied the dynamics of each ion species in the moon's magnetosphere and pick-up tail.

Our major results are as follows:

1. The magnetic field perturbations observed along Juno's flyby trajectory are dominated by Ganymede's internal dipole and its interaction with the impinging Jovian magnetospheric flow. The magnetic perturbations are dominated by plasma currents only within the observed “wake” region (Allegrini et al., 2022). Regardless of the chosen level of complexity, Ganymede's ionosphere produces only subtle signatures in the magnetic field along Juno's trajectory.
2. The O₂⁺ pick-up ions populate the region dominated by Ganymede's internal field and form a tail with steep boundaries along its Jupiter-facing and Jupiter-averted flanks. The O₂⁺ ions are only able to penetrate the moon's Jupiter-averted ($y < 0$) magnetopause due to their large gyroradii (about $0.2 R_G$).

3. Flow shear between ionospheric O_2^+ ions and the Jovian magnetospheric plasma generates signatures of Kelvin-Helmholtz instability (KHI) along the Jupiter-facing ($y > 0$) flank of Ganymede's magnetopause. The KHI introduces quasi-periodic "breathing" of the Jupiter-facing magnetopause location, which moves in and out from Ganymede by about $0.15 R_G$ over a period of approximately 5 min. In the outbound segment of Juno's flyby, the spacecraft passed through this region affected by KHI, indicating that the observed magnetopause crossing only provides a snapshot in time of the Jupiter-facing magnetopause location. Had the flyby occurred a few minutes earlier or later, our results suggest that the outbound magnetopause crossing may have been offset by up to $0.15 R_G$ in either direction along the trajectory.
4. Due to the large scale height of atmospheric H_2 (about $0.4 R_G$), a significant amount of H_2^+ ions are produced outside of Ganymede's magnetopause. These ions form a dilute "corona" around the moon's magnetosphere. The inclusion of H_2 (setup III), dayside photo-ionization (setup IV), and H_2O (setup V) all yield only minimal quantitative changes in the structure of Ganymede's magnetosphere and plasma tail. The modeled O_2^+ and H_2^+ densities both closely match the time series observed by Juno's JADE instrument within Ganymede's magnetosphere.
5. Ganymede's H_2O^+ pick-up tail is very dilute, possessing number densities two orders of magnitude below those of the O_2^+ tail. Due to the small scale height of H_2O and the location of Ganymede's subsolar point in the equatorial plane (about which the H_2O bulge is centered), most of the H_2O^+ ion production occurs within the closed field line region. Such ions are mostly unable to escape toward downstream and therefore cannot contribute to the moon's pick-up tail.
6. In our model, the total ionospheric outflow is dominated by O_2^+ , with approximately $10^{27} O_2^+$ ions/s (53 kg/s) escaping Ganymede's magnetosphere. The outflow rates are about 10^{26} ions/s (0.3 kg/s) and 10^{24} ions/s (0.03 kg/s) for ionospheric H_2^+ and H_2O^+ , respectively.

We look forward to applying our Ganymede model in support of the recently launched JUICE spacecraft, set to enter orbit around the moon in 2034.

Appendix A: Model Validation: Comparison to Galileo Magnetometer Data

To validate the AIKEF hybrid code (introduced in Section 2.1) for modeling Ganymede's near-space environment, we apply the model to study magnetometer observations from all six Galileo flybys of the moon (see Figure 1). We compare the magnetic field components produced by the model to magnetometer data along each flyby trajectory. The model setups for the six Galileo flybys include Ganymede's permanent and induced magnetic dipole moments (see Table A1). However, for this series of simulations, we proceed analogous to the hybrid modeling studies of Fatemi et al. (2016, 2022) and Poppe et al. (2018) and do not include the moon's atmosphere or ionosphere.

In each model setup, we assume a uniform background magnetic field \mathbf{B}_0 with values adopted from Kivelson et al. (2002), see Table A1. For Ganymede's permanent magnetic dipole moment, we adopt the value determined by Kivelson et al. (2002) and described in Section 2.2 (see Table A1). The moon's inductive response is calculated in the same way as described in Section 2.2 (see Equation 2). With the exception of the Jovian plasma density, which varies as a function of Ganymede's distance to the center of Jupiter's magnetospheric plasma sheet, we adopt the same upstream parameters as described in Section 2.2. We use a number density of $n_0 = 4 \text{ cm}^{-3}$ when Ganymede is located far from the center of the Jovian plasma sheet (G1, G2, G7, G28, and G29), and a value of $n_0 = 8 \text{ cm}^{-3}$ when the moon is located close to the center of the sheet (G8). These number densities are consistent with the range of $1\text{--}10 \text{ cm}^{-3}$ provided in Jia and Kivelson (2021) and similar to the input parameters chosen in the model of Fatemi et al. (2022).

In Figure A1, we present the magnetic field components produced by the AIKEF model along the six Galileo trajectories and compare them to magnetometer observations. As can be seen, the model achieves very good quantitative agreement with both the magnitudes and locations of the observed magnetic field perturbations for all three components. This further emphasizes that AIKEF is highly suitable to analyze Ganymede's magnetospheric interaction during the PJ34 Juno flyby. We refrain from providing a detailed discussion of the model-data comparisons shown in Figure A1. Similar comparisons for the Galileo flybys have already been performed and analyzed in detail by numerous preceding studies (e.g., Duling et al., 2014; Fatemi et al., 2016, 2022; Jia et al., 2008, 2009). Therefore, another extensive discussion would not produce any novel physical insights.

Table A1
Simulation Parameters of the AKEF Model for the Six Galileo Flybys of Ganymede

Parameter	Symbol (units)	G1	G2	G7	G8	G28	G29
Background magnetic field ^a	\mathbf{B}_0 (nT)	(6, -79, -79)	(17, -73, -85)	(-3, 84, -75)	(-11, 11, -77)	(-7, 78, -76)	(-9, -83, -79)
Background field magnitude ^a	B_0 (nT)	111.9	113.3	113.3	78.6	109.1	114.9
Ganymede's Magnetic moment (permanent) ^a	\mathbf{M}_{dip} ($\times 10^{27}$ JnT)	(-4.1, 9.0, -131.0)	(-4.1, 9.0, -131.0)	(-4.1, 9.0, -131.0)	(-4.1, 9.0, -131.0)	(-4.1, 9.0, -131.0)	(-4.1, 9.0, -131.0)
Ganymede's Magnetic moment (induced) ^a	\mathbf{M}_{ind} ($\times 10^{27}$ JnT)	(-0.5, 6.1, 0.0)	(-1.3, 5.6, 0.0)	(0.2, -6.4, 0.0)	(0.7, 0.5, 0.0)	(0.5, -6.0, 0.0)	(0.7, 6.4, 0.0)
Upstream plasma number density ^b	n_0 (cm ⁻³)	4	4	4	8	4	4
Upstream plasma mean ion mass ^b	m_0 (amu)	14	14	14	14	14	14
Upstream plasma bulk velocity ^b	\mathbf{u}_0 (km/s)	(140,0,0)	(140,0,0)	(130,0,0)	(140,0,0)	(140,0,0)	(140,0,0)
Upstream plasma ion temperature ^b	$k_B T_0$ (eV)	100	100	100	100	100	100
Upstream plasma electron temperature ^b	$k_B T_0$ (eV)	100	100	100	100	100	100
Convective electric field ^c ($\mathbf{E}_0 = -\mathbf{u}_0 \times \mathbf{B}_0$)	\mathbf{E}_0 (mV/m)	(0, -11.1, 11.1)	(0, -11.9, 10.2)	(0, -9.9, -10.9)	(0, -10.8, -1.5)	(0, -10.6, -10.9)	(0, -11.1, 11.6)
Alfvén velocity ($V_{A,0} = \frac{B_0}{\sqrt{\mu_0 n_0 n_0}}$) ^c	$V_{A,0}$ (km/s)	326	330	330	162	318	335
Alfvén Mach number ($M_{A,0} = \frac{u_0}{V_{A,0}}$) ^c	$M_{A,0}$	0.43	0.42	0.39	0.87	0.44	0.42

^aKivelson et al. (2002). ^bKivelson et al. (2004). ^c(Calculated).

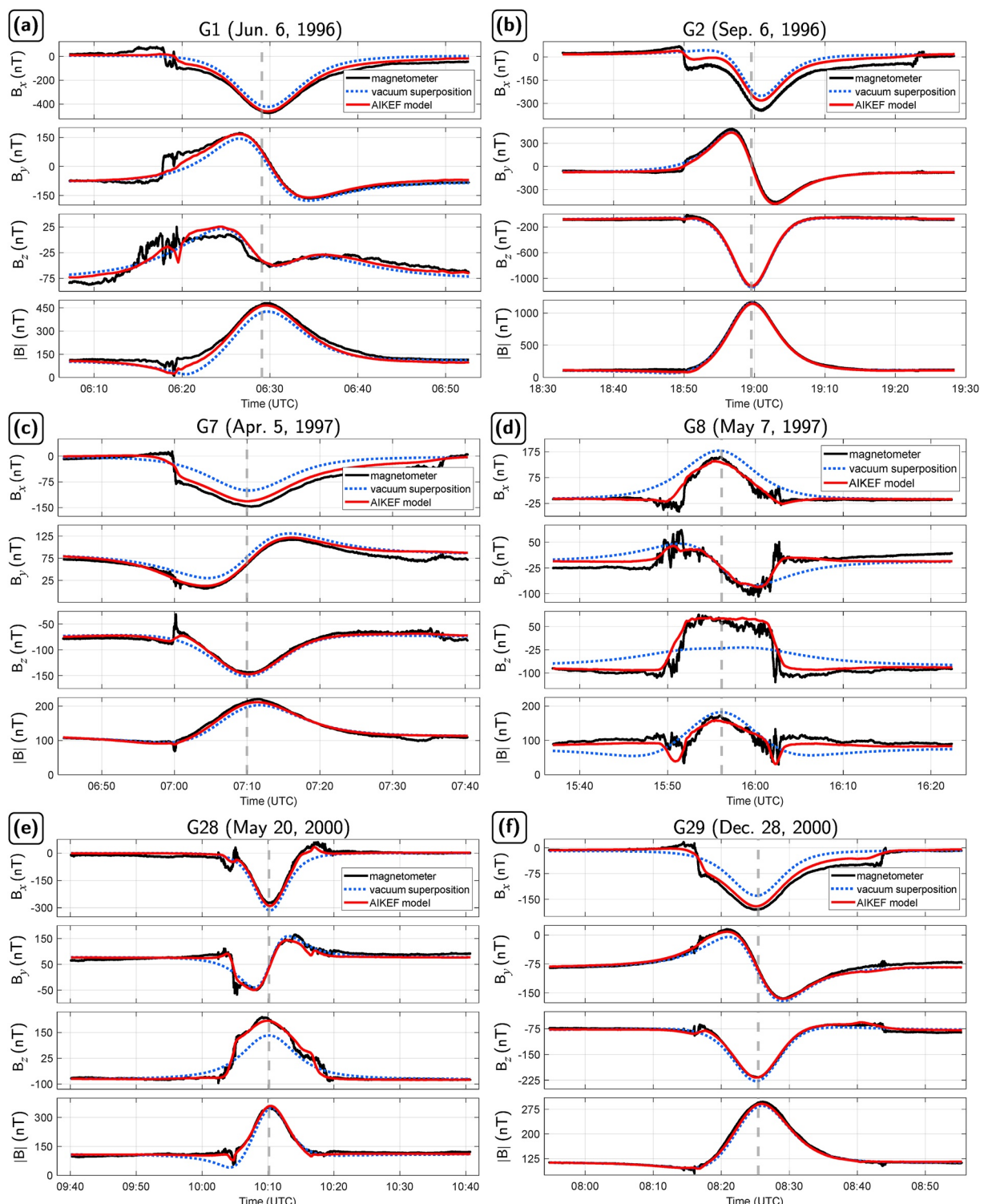


Figure A1. Comparisons of modeled magnetic field components (presented in GPhiO coordinates) from AIKEF (red lines) to Galileo magnetometer observations (black lines) for the six flybys of Ganymede. The flybys are labeled as follows: (a) for G1, (b) for G2, (c) for G7, (d) for G8, (e) for G28, and (f) for G29. In addition to the AIKEF output, we show the magnetic field components obtained by mere superposition of Ganymede's internal field and the magnetospheric background field (called "vacuum superposition" by Kivelson et al. (2002); blue dotted lines). Galileo's closest approach to Ganymede is denoted by a vertical gray dashed line for each flyby. Parameters used for the AIKEF model setup of each flyby can be found in Table A1. Each run includes Ganymede's permanent and induced magnetic dipoles. However, analogous to the approach of Fatemi et al. (2016, 2022) and Poppe et al. (2018), these model runs do not take into account an atmosphere or ionosphere.

Data Availability Statement

The data supporting this work can be obtained from Stahl et al. (2023).

Acknowledgments

The authors are grateful to the NASA Solar System Workings 2018 Program (Grant 80NSSC20K0463) for financial support. We would also like to thank Tyler Tippens and C. Michael Haynes (both at the Georgia Institute of Technology) for helpful input on various aspects of this project.

References

- Addison, P., Liuzzo, L., Arnold, H., & Simon, S. (2021). Influence of Europa's time-varying electromagnetic environment on magnetospheric ion precipitation and surface weathering. *Journal of Geophysical Research: Space Physics*, 126(5), e2020JA029087. <https://doi.org/10.1029/2020JA029087>
- Addison, P., Liuzzo, L., & Simon, S. (2022). Effect of the magnetospheric plasma interaction and solar illumination on ion sputtering of Europa's surface ice. *Journal of Geophysical Research: Space Physics*, 127(2), e2021JA030136. <https://doi.org/10.1029/2021JA030136>
- Addison, P., Liuzzo, L., & Simon, S. (2023). Surface-plasma interactions at Europa in draped magnetospheric fields: The contribution of energetic electrons to energy deposition and sputtering. *Journal of Geophysical Research: Space Physics*, 128(8), e2023JA031734. <https://doi.org/10.1029/2023JA031734>
- Alday, J., Roth, L., Ivchenko, N., Retherford, K. D., Becker, T. M., Molyneux, P., & Saur, J. (2017). New constraints on Ganymede's hydrogen corona: Analysis of Lyman-alpha emissions observed by HST/STIS between 1998 and 2014. *Planetary and Space Science*, 148, 35–44. <https://doi.org/10.1016/j.pss.2017.10.006>
- Allegrini, F., Bagenal, F., Ebert, R., Louarn, P., Mccomas, D., Szalay, J., et al. (2022). Plasma observations during the June 7, 2021 Ganymede flyby from the Jovian Auroral Distributions Experiment (JADE) on Juno. *Geophysical Research Letters*, 49(23), e2022GL098682. <https://doi.org/10.1029/2022GL098682>
- Anderson, J. D., Lau, E. L., Sjogren, W. L., Schubert, G., & Moore, W. B. (1996). Gravitational constraints on the internal structure of Ganymede. *Nature*, 384(6609), 541–543. <https://doi.org/10.1038/384541a0>
- Arnold, H., Liuzzo, L., & Simon, S. (2019). Magnetic signatures of a plume at Europa during the Galileo E26 flyby. *Geophysical Research Letters*, 46(3), 1149–1157. <https://doi.org/10.1029/2018GL081544>
- Arnold, H., Liuzzo, L., & Simon, S. (2020). Plasma interaction signatures of plumes at Europa. *Journal of Geophysical Research: Space Physics*, 125(1), e2019JA027346. <https://doi.org/10.1029/2019JA027346>
- Arnold, H., Simon, S., & Liuzzo, L. (2020). Applying ion energy spectrograms to search for plumes at Europa. *Journal of Geophysical Research: Space Physics*, 125(9), e2020JA028376. <https://doi.org/10.1029/2020JA028376>
- Bagenal, F., & Delamere, P. A. (2011). Flow of mass and energy in the magnetospheres of Jupiter and Saturn. *Journal of Geophysical Research*, 116(A5), A05209. <https://doi.org/10.1029/2010JA016294>
- Bagenal, F., Wilson, R. J., Siler, S., Paterson, W. R., & Kurth, W. S. (2016). Survey of Galileo plasma observations in Jupiter's plasma sheet. *Journal of Geophysical Research: Planets*, 121(5), 871–894. <https://doi.org/10.1002/2016JE005009>
- Bonfond, B., Hess, S., Bagenal, F., Gérard, J.-C., Grodent, D., Radioti, A., et al. (2013). The multiple spots of the Ganymede auroral footprint. *Geophysical Research Letters*, 40(19), 4977–4981. <https://doi.org/10.1002/grl.50989>
- Bonfond, B., Saur, J., Grodent, D., Badman, S. V., Bisikalo, D., Shematovich, V., et al. (2017). The tails of the satellite auroral footprints at Jupiter. *Journal of Geophysical Research: Space Physics*, 122(8), 7985–7996. <https://doi.org/10.1002/2017JA024370>
- Breer, B. R., Liuzzo, L., Arnold, H., Andersson, P. N., & Simon, S. (2019). Energetic ion dynamics in the perturbed electromagnetic fields near Europa. *Journal of Geophysical Research: Space Physics*, 124(9), 7592–7613. <https://doi.org/10.1029/2019JA027147>
- Buccino, D. R., Parisi, M., Gramigna, E., Gomez-Casajus, L., Tortora, P., Zannoni, M., et al. (2022). Ganymede's ionosphere observed by a dual-frequency radio occultation with Juno. *Geophysical Research Letters*, 49(23), e2022GL098420. <https://doi.org/10.1029/2022GL098420>
- Carberry Mogan, S. R., Johnson, R. E., Vorburger, A., & Roth, L. (2023). Electron impact ionization in the icy Galilean satellites' atmospheres. *European Physical Journal D: Atomic, Molecular and Optical Physics*, 77(2), 26. <https://doi.org/10.1140/epjd/s10053-023-00606-8>
- Carnielli, G., Galand, M., Leblanc, F., Leclercq, L., Modolo, R., Beth, A., et al. (2019). First 3D test particle model of Ganymede's ionosphere. *Icarus*, 330, 42–59. <https://doi.org/10.1016/j.icarus.2019.04.016>
- Carnielli, G., Galand, M., Leblanc, F., Modolo, R., Beth, A., & Jia, X. (2020). Constraining Ganymede's neutral and plasma environments through simulations of its ionosphere and Galileo observations. *Icarus*, 343, 113691. <https://doi.org/10.1016/j.icarus.2020.113691>
- Cervantes, S., & Saur, J. (2022). Constraining Europa's subsolar atmosphere with a joint analysis of HST spectral images and Galileo magnetic field data. *Journal of Geophysical Research: Space Physics*, 127(9), e2022JA030472. <https://doi.org/10.1029/2022JA030472>
- Clark, G., Kollmann, P., Mauk, B. H., Paranicas, C., Haggerty, D., Rymer, A., et al. (2022). Energetic charged particle observations during Juno's close flyby of Ganymede. *Geophysical Research Letters*, 49(23), e2022GL098572. <https://doi.org/10.1029/2022GL098572>
- Coates, A. J., Wellbrock, A., Lewis, G. R., Arridge, C. S., Crary, F. J., Young, D. T., et al. (2012). Cassini in Titan's tail: CAPS observations of plasma escape. *Journal of Geophysical Research*, 117(A5), A05324. <https://doi.org/10.1029/2012JA017595>
- Connerney, J. E. P., Benn, M., Bjarno, J., Denver, T., Espley, J., Jorgenson, J., et al. (2017). The Juno magnetic field investigation. *Space Science Reviews*, 213(1–4), 39–138. <https://doi.org/10.1007/s11214-017-0334-z>
- Connerney, J. E. P., Adriani, A., Allegrini, F., Bagenal, F., Bolton, S. J., Bonfond, B., et al. (2017). Jupiter's magnetosphere and aurorae observed by the Juno spacecraft during its first polar orbits. *Science*, 356(6340), 826–832. <https://doi.org/10.1126/science.aam5928>
- Cooper, J. F., Johnson, R. E., Mauk, B. H., Garrett, H. B., & Gehrels, N. (2001). Energetic ion and electron irradiation of the icy Galilean satellites. *Icarus*, 149(1), 133–159. <https://doi.org/10.1006/icar.2000.6498>
- Dorelli, J. C., Gloeck, A., Collinson, G., & Tóth, G. (2015). The role of the Hall effect in the global structure and dynamics of planetary magnetospheres: Ganymede as a case study. *Journal of Geophysical Research A: Space Physics*, 120(7), 5377–5392. <https://doi.org/10.1002/2014JA020951>
- Duling, S., Saur, J., Clark, G., Allegrini, F., Greathouse, T., Gladstone, R., et al. (2022). Ganymede MHD model: Magnetospheric context for Juno's PJ34 flyby. *Geophysical Research Letters*, 49(24), e2022GL101688. <https://doi.org/10.1029/2022GL101688>
- Duling, S., Saur, J., & Wicht, J. (2014). Consistent boundary conditions at nonconducting surfaces of planetary bodies: Applications in a new Ganymede MHD model. *Journal of Geophysical Research: Space Physics*, 119(6), 4412–4440. <https://doi.org/10.1002/2013JA019554>
- Eviatar, A., Strobel, D. F., Wolven, B. C., Feldman, P. D., McGrath, M. A., & Williams, D. J. (2001). Excitation of the Ganymede ultraviolet aurora. *The Astrophysical Journal*, 555(2), 1013–1019. <https://doi.org/10.1086/321510>
- Eviatar, A., Vasylunas, V. M., & Gurnett, D. A. (2001). The ionosphere of Ganymede. *Planetary and Space Science*, 49(3–4), 327–336. [https://doi.org/10.1016/S0032-0633\(00\)00154-9](https://doi.org/10.1016/S0032-0633(00)00154-9)
- Eviatar, A., Williams, D. J., Paranicas, C., McEntire, R. W., Mauk, B. H., & Kivelson, M. G. (2000). Trapped energetic electrons in the magnetosphere of Ganymede. *Journal of Geophysical Research*, 105(A3), 5547–5553. <https://doi.org/10.1029/1999ja00450>

- Fatemi, S., Poppe, A. R., Khurana, K. K., Holmström, M., & Delory, G. T. (2016). On the formation of Ganymede's surface brightness asymmetries: Kinetic simulations of Ganymede's magnetosphere. *Geophysical Research Letters*, 43(10), 4745–4754. <https://doi.org/10.1002/2016GL068363>
- Fatemi, S., Poppe, A. R., Vorburger, A., Lindkvist, J., & Hamrin, M. (2022). Ion dynamics at the magnetopause of Ganymede. *Journal of Geophysical Research: Space Physics*, 127(1), e2021JA029863. <https://doi.org/10.1029/2021JA029863>
- Feldman, P. D., McGrath, M. A., Strobel, D. F., Moos, H. W., Retherford, K. D., & Woven, B. C. (2000). HST/STIS ultraviolet imaging of polar aurora on Ganymede. *The Astrophysical Journal*, 535(2), 1085–1090. <https://doi.org/10.1086/308889>
- Feyerabend, M., Simon, S., Motschmann, U., & Liuzzo, L. (2015). Filamented ion tail structures at Titan: A hybrid simulation study. *Planetary and Space Science*, 117, 362–376. <https://doi.org/10.1016/j.pss.2015.07.008>
- Frank, L. A., Paterson, W. R., Ackerson, K. L., & Bolton, S. J. (1997). Low-energy electron measurements at Ganymede with the Galileo spacecraft: Probes of the magnetic topology. *Geophysical Research Letters*, 24(17), 2159–2162. <https://doi.org/10.1029/97GL01632>
- Greathouse, T. K., Gladstone, G. R., Molyneux, P. M., Versteeg, M. H., Hue, V., Kammer, J. A., et al. (2022). UV observations of Ganymede's aurora during Juno orbits 34 and 35. *Geophysical Research Letters*, 49(23), e2022GL099794. <https://doi.org/10.1029/2022GL099794>
- Grodent, D., Bonfond, B., Radioti, A., Gérard, J.-C., Jia, X., Nichols, J. D., & Clarke, J. T. (2009). Auroral footprint of Ganymede. *Journal of Geophysical Research*, 114(A7), A07212. <https://doi.org/10.1029/2009JA014289>
- Gurnett, D. A., Kurth, W. S., Roux, A., Bolton, S. J., & Kennel, C. F. (1996). Evidence for a magnetosphere at Ganymede from plasma-wave observations by the Galileo spacecraft. *Nature*, 384(6609), 535–537. <https://doi.org/10.1038/384535a0>
- Hall, D. T., Feldman, P. D., McGrath, M. A. M. A., & Strobel, D. F. (1998). The far-ultraviolet oxygen airglow of Europa and Ganymede. *The Astrophysical Journal*, 499(1), 475–481. <https://doi.org/10.1086/305604>
- Hansen, C. J., Bolton, S., Sulaiman, A. H., Duling, S., Bagenal, F., Brennan, M., et al. (2022). Juno's close encounter with Ganymede—An overview. *Geophysical Research Letters*, 49(23), e2022GL099285. <https://doi.org/10.1029/2022GL099285>
- Hue, V., Szalay, J. R., Greathouse, T. K., Bonfond, B., Kotsiaros, S., Louis, C. K., et al. (2022). A comprehensive set of Juno in situ and remote sensing observations of the Ganymede auroral footprint. *Geophysical Research Letters*, 49(7), e2021GL096994. <https://doi.org/10.1029/2021GL096994>
- Ip, W.-H., & Kopp, A. (2002). Resistive MHD simulations of Ganymede's magnetosphere 2. Birkeland currents and particle energetics. *Journal of Geophysical Research*, 107(A12), SMP42-1–SMP42-7. <https://doi.org/10.1029/2001JA005072>
- Jia, X., & Kivelson, M. G. (2021). The magnetosphere of Ganymede. In *Magnetospheres in the solar system* (pp. 557–573). American Geophysical Union (AGU). <https://doi.org/10.1002/9781119815624.ch35>
- Jia, X., Walker, R. J., Kivelson, M. G., Khurana, K. K., & Linker, J. A. (2008). Three-dimensional MHD simulations of Ganymede's magnetosphere. *Journal of Geophysical Research*, 113(6), A06212. <https://doi.org/10.1029/2007JA012748>
- Jia, X., Walker, R. J., Kivelson, M. G., Khurana, K. K., & Linker, J. A. (2009). Properties of Ganymede's magnetosphere inferred from improved three-dimensional MHD simulations. *Journal of Geophysical Research*, 114(9), A09209. <https://doi.org/10.1029/2009JA014375>
- Jia, X., Walker, R. J., Kivelson, M. G., Khurana, K. K., & Linker, J. A. (2010). Dynamics of Ganymede's magnetopause: Intermittent reconnection under steady external conditions. *Journal of Geophysical Research*, 115(12), A12202. <https://doi.org/10.1029/2010JA015771>
- Joy, S. P., Kivelson, M. G., Walker, R. J., Khurana, K. K., Russell, C. T., & Ogino, T. (2002). Probabilistic models of the Jovian magnetopause and bow shock locations. *Journal of Geophysical Research*, 107(A10), 1309. <https://doi.org/10.1029/2001JA009146>
- Kaweeyanun, N., Masters, A., & Jia, X. (2020). Favorable conditions for magnetic reconnection at Ganymede's upstream magnetopause. *Geophysical Research Letters*, 47(6), 0–3. <https://doi.org/10.1029/2019GL086228>
- Kaweeyanun, N., Masters, A., & Jia, X. (2021). Analytical assessment of Kelvin-Helmholtz instability growth at Ganymede's upstream magnetopause. *Journal of Geophysical Research: Space Physics*, 126(8), e2021JA029338. <https://doi.org/10.1029/2021JA029338>
- Khurana, K. K., Pappalardo, R., Murphy, N., & Denk, T. (2007). The origin of Ganymede's polar caps. *Icarus*, 191(1), 193–202. <https://doi.org/10.1016/j.icarus.2007.04.022>
- Kim, T. K., Ebert, R. W., Valek, P. W., Allegrini, F., McComas, D. J., Bagenal, F., et al. (2020). Survey of ion properties in Jupiter's plasma sheet: Juno JADE-I observations. *Journal of Geophysical Research: Space Physics*, 125(4), e2019JA027696. <https://doi.org/10.1029/2019JA027696>
- Kivelson, M., Bagenal, F., Kurth, W., Neubauer, F., Paranicas, C., & Saur, J. (2004). Magnetospheric interactions with satellites. *Jupiter: The Planet, Satellites and Magnetosphere*, 513–536.
- Kivelson, M., Khurana, K. K., Russell, C. T., Walker, R. J., Warnecke, J., Coroniti, F. V., et al. (1996). Discovery of Ganymede's magnetic field by the Galileo spacecraft. *Nature*, 384(6609), 537–541. <https://doi.org/10.1038/384537a0>
- Kivelson, M., Khurana, K. K., & Volwerk, M. (2002). The permanent and inductive magnetic moments of Ganymede. *Icarus*, 157(2), 507–522. <https://doi.org/10.1006/icar.2002.6834>
- Kivelson, M., Warnecke, J., Bennett, L., Joy, S., Khurana, K. K., Linker, J. A., et al. (1998). Ganymede's magnetosphere: Magnetometer overview. *Journal of Geophysical Research*, 103(E9), 19963–19972. <https://doi.org/10.1029/98JE00227>
- Kliore, A. J. (1998). Satellite atmospheres and magnetospheres. In J. Andersen (Ed.), *Highlights of astronomy: As presented at the XXIIIRD general assembly of the IAU, 1997* (pp. 1065–1069). Springer Netherlands. https://doi.org/10.1007/978-94-011-4778-1_138
- Kriegel, H., Simon, S., Meier, P., Motschmann, U., Saur, J., Wennmacher, A., et al. (2014). Ion densities and magnetic signatures of dust pick-up at Enceladus. *Journal of Geophysical Research: Space Physics*, 119(4), 2740–2774. <https://doi.org/10.1002/2013JA019440>
- Kriegel, H., Simon, S., Motschmann, U., Saur, J., Neubauer, F. M., Persoon, A. M., et al. (2011). Influence of negatively charged plume grains on the structure of Enceladus' Alfvén wings: Hybrid simulations versus Cassini magnetometer data. *Journal of Geophysical Research*, 116(10), 1–19. <https://doi.org/10.1029/2011JA016842>
- Krupp, N., Vasiliunas, V., Woch, J., Lagg, A., Khurana, K., Kivelson, M., et al. (2004). The dynamics of the Jovian magnetosphere. *Jupiter: The Planet, Satellites and Magnetosphere*, 617–638.
- Kurth, W., Hospodarsky, G., Kirchner, D., Mokrzycki, B., Averkamp, T., Robison, W., et al. (2017). The Juno waves investigation. *Space Science Reviews*, 213(1–4), 347–392. <https://doi.org/10.1007/s11214-017-0396-y>
- Kurth, W. S., Sulaiman, A. H., Hospodarsky, G. B., Menietti, J. D., Mauk, B. H., Clark, G., et al. (2022). Juno plasma wave observations at Ganymede. *Geophysical Research Letters*, 49(23), e2022GL098591. <https://doi.org/10.1029/2022GL098591>
- Leblanc, F., Oza, A. V., Leclercq, L., Schmidt, C., Cassidy, T., Modolo, R., et al. (2017). On the orbital variability of Ganymede's atmosphere. *Icarus*, 293, 185–198. <https://doi.org/10.1016/j.icarus.2017.04.025>
- Leblanc, F., Roth, L., Chaufray, J., Modolo, R., Galand, M., Ivchenko, N., et al. (2023). Ganymede's atmosphere as constrained by HST/STIS observations. *Icarus*, 399, 115557. <https://doi.org/10.1016/j.icarus.2023.115557>
- Liuzzo, L., Feyerabend, M., Simon, S., & Motschmann, U. (2015). The impact of Callisto's atmosphere on its plasma interaction with the Jovian magnetosphere. *Journal of Geophysical Research A: Space Physics*, 120(11), 9401–9427. <https://doi.org/10.1002/2015JA021792>
- Liuzzo, L., Poppe, A. R., Addison, P., Simon, S., Nénon, Q., & Paranicas, C. (2022). Energetic magnetospheric particle fluxes onto Callisto's atmosphere. *Journal of Geophysical Research: Space Physics*, 127(11), e2022JA030915. <https://doi.org/10.1029/2022JA030915>

- Liuzzo, L., Poppe, A. R., Paranicas, C., Nénon, Q., Fatemi, S., & Simon, S. (2020). Variability in the energetic electron bombardment of Ganymede. *Journal of Geophysical Research: Space Physics*, 125(9), e2020JA028347. <https://doi.org/10.1029/2020JA028347>
- Liuzzo, L., Simon, S., & Feyerabend, M. (2018). Observability of Callisto's inductive signature during the JUpiter ICY Moons explorer mission. *Journal of Geophysical Research: Space Physics*, 123(11), 9045–9054. <https://doi.org/10.1029/2018JA025951>
- Liuzzo, L., Simon, S., Feyerabend, M., & Motschmann, U. (2016). Disentangling plasma interaction and induction signatures at Callisto: The Galileo C10 flyby. *Journal of Geophysical Research: Space Physics*, 121(9), 8677–8694. <https://doi.org/10.1002/2016JA023236>
- Liuzzo, L., Simon, S., Feyerabend, M., & Motschmann, U. (2017). Magnetic signatures of plasma interaction and induction at Callisto: The Galileo C21, C22, C23, and C30 flybys. *Journal of Geophysical Research: Space Physics*, 122(7), 7364–7386. <https://doi.org/10.1002/2017JA024303>
- Liuzzo, L., Simon, S., & Regoli, L. (2019a). Energetic electron dynamics near Callisto. *Planetary and Space Science*, 179, 104726. <https://doi.org/10.1016/j.pss.2019.104726>
- Liuzzo, L., Simon, S., & Regoli, L. (2019b). Energetic ion dynamics near Callisto. *Planetary and Space Science*, 166, 23–53. <https://doi.org/10.1016/j.pss.2018.07.014>
- Marconi, M. L. (2007). A kinetic model of Ganymede's atmosphere. *Icarus*, 190(1), 155–174. <https://doi.org/10.1016/j.icarus.2007.02.016>
- Masters, A. (2017). Model-based assessments of magnetic reconnection and Kelvin-Helmholtz instability at Jupiter's magnetopause. *Journal of Geophysical Research: Space Physics*, 122(11), 11154–11174. <https://doi.org/10.1002/2017JA024736>
- Mauk, B. H., Mitchell, D. G., McEntire, R. W., Paranicas, C. P., Roelof, E. C., Williams, D. J., et al. (2004). Energetic ion characteristics and neutral gas interactions in Jupiter's magnetosphere. *Journal of Geophysical Research*, 109(A9), A09S12. <https://doi.org/10.1029/2003JA010270>
- McComas, D. J., Alexander, N., Allegrini, F., Bagenal, F., Beebe, C. R., Clark, G., et al. (2017). The Jovian Auroral Distributions Experiment (JADE) on the Juno mission to Jupiter. *Space Science Reviews*, 213(1–4), 547–643. <https://doi.org/10.1007/s11214-013-9990-9>
- McGrath, M. A., Jia, X., Retherford, K., Feldman, P. D., Strobel, D. F., & Saur, J. (2013). Aurora on Ganymede. *Journal of Geophysical Research: Space Physics*, 118(5), 2043–2054. <https://doi.org/10.1002/jgra.50122>
- Molyneux, P. M., Nichols, J. D., Bannister, N. P., Bunce, E. J., Clarke, J. T., Cowley, S. W. H., et al. (2018). Hubble space telescope observations of variations in Ganymede's oxygen atmosphere and aurora. *Journal of Geophysical Research: Space Physics*, 123(5), 3777–3793. <https://doi.org/10.1029/2018JA025243>
- Müller, J., Simon, S., Motschmann, U., Schüle, J., Glassmeier, K. H., & Pringle, G. J. (2011). A.I.K.E.F.: Adaptive hybrid model for space plasma simulations. *Computer Physics Communications*, 182(4), 946–966. <https://doi.org/10.1016/j.cpc.2010.12.033>
- Müller, J., Simon, S., Wang, Y.-C., Motschmann, U., Heyner, D., Schüle, J., et al. (2012). Origin of Mercury's double magnetopause: 3D hybrid simulation study with A.I.K.E.F. *Icarus*, 218(1), 666–687. <https://doi.org/10.1016/j.icarus.2011.12.028>
- Neubauer, F. M. (1980). Nonlinear standing Alfvén wave current system at Io: Theory. *Journal of Geophysical Research*, 85(9), 1171–1178. <https://doi.org/10.1029/JA085iA03p01171>
- Neubauer, F. M. (1998). The sub-Alfvénic interaction of the Galilean satellites with the Jovian magnetosphere. *Journal of Geophysical Research*, 103(E9), 19843–19866. <https://doi.org/10.1029/97JE03370>
- Neubauer, F. M. (1999). Alfvén wings and electromagnetic induction in the interiors: Europa and Callisto. *Journal of Geophysical Research*, 104(A12), 28671–28684. <https://doi.org/10.1029/1999JA000217>
- Paty, C., Paterson, W., & Winglee, R. (2008). Ion energization in Ganymede's magnetosphere: Using multifluid simulations to interpret ion energy spectrograms. *Journal of Geophysical Research*, 113(6), A06211. <https://doi.org/10.1029/2007JA012848>
- Paty, C., & Winglee, R. (2004). Multi-fluid simulations of Ganymede's magnetosphere. *Geophysical Research Letters*, 31(24), 1–5. <https://doi.org/10.1029/2004GL021220>
- Paty, C., & Winglee, R. (2006). The role of ion cyclotron motion at Ganymede: Magnetic field morphology and magnetospheric dynamics. *Geophysical Research Letters*, 33(10), L10106. <https://doi.org/10.1029/2005GL025273>
- Payan, A. P., Paty, C. S., & Retherford, K. D. (2015). Uncovering local magnetospheric processes governing the morphology and variability of Ganymede's aurora using three-dimensional multifluid simulations of Ganymede's magnetosphere. *Journal of Geophysical Research: Space Physics*, 120(1), 401–413. <https://doi.org/10.1002/2014JA020301>
- Plainaki, C., Milillo, A., Massetti, S., Mura, A., Jia, X., Orsini, S., et al. (2015). The H₂O and O₂ exospheres of Ganymede: The result of a complex interaction between the Jovian magnetospheric ions and the icy moon. *Icarus*, 245, 306–319. <https://doi.org/10.1016/j.icarus.2014.09.018>
- Poppe, A. R., Fatemi, S., & Khurana, K. K. (2018). Thermal and energetic ion dynamics in Ganymede's magnetosphere. *Journal of Geophysical Research: Space Physics*, 123(6), 4614–4637. <https://doi.org/10.1029/2018JA025312>
- Romanelli, N., DiBraccio, G. A., Modolo, R., Connerney, J. E. P., Ebert, R. W., Martos, Y. M., et al. (2022). Juno magnetometer observations at Ganymede: Comparisons with a global hybrid simulation and indications of magnetopause reconnection. *Geophysical Research Letters*, 49(23), e2022GL099545. <https://doi.org/10.1029/2022GL099545>
- Roth, L. (2021). A stable H₂O atmosphere on Europa's trailing hemisphere from HST images. *Geophysical Research Letters*, 48(20), e2021GL094289. <https://doi.org/10.1029/2021GL094289>
- Roth, L., Ivchenko, N., Gladstone, G., Saur, J., Grodent, D., Bonfond, B., et al. (2021). A sublimated water atmosphere on Ganymede detected from Hubble Space Telescope observations. *Nature Astronomy*, 5(10), 1043–1051. <https://doi.org/10.1038/s41550-021-01426-9>
- Roth, L., Marchesini, G., Becker, T. M., Hoeijmakers, H. J., Molyneux, P. M., Retherford, K. D., et al. (2023). Probing Ganymede's atmosphere with HST Ly-alpha images in Transit of Jupiter. *The Planetary Science Journal*, 4(1), 12. <https://doi.org/10.3847/PSJ/acaf7f>
- Saur, J., Duling, S., Roth, L., Jia, X., Strobel, D. F., Feldman, P. D., et al. (2015). The search for a subsurface ocean in Ganymede with Hubble Space Telescope observations of its auroral ovals. *Journal of Geophysical Research: Space Physics*, 120(3), 1715–1737. <https://doi.org/10.1002/2014JA020778>
- Saur, J., Neubauer, F. M., & Glassmeier, K.-H. H. (2010). Induced magnetic fields in solar system bodies. *Space Science Reviews*, 152(1–4), 391–421. <https://doi.org/10.1007/s11214-009-9581-y>
- Schubert, G., Zhang, K., Kivelson, M. G., & Anderson, J. D. (1996). The magnetic field and internal structure of Ganymede. *Nature*, 384(6609), 544–545. <https://doi.org/10.1038/384544a0>
- Shematovich, V. (2016). Neutral atmosphere near the icy surface of Jupiter's moon Ganymede. *Solar System Research*, 50(4), 262–280. <https://doi.org/10.1134/S0038094616040067>
- Simon, S., Addison, P., & Liuzzo, L. (2022). Formation of a displaced plasma wake at Neptune's Moon Triton. *Journal of Geophysical Research: Space Physics*, 127(1), e2021JA029958. <https://doi.org/10.1029/2021JA029958>
- Simon, S., Boesswetter, A., Bagdonat, T., Motschmann, U., & Schuele, J. (2007). Three-dimensional multispecies hybrid simulation of Titan's highly variable plasma environment. *Annales Geophysicae*, 25(1), 117–144. <https://doi.org/10.5194/angeo-25-117-2007>
- Stahl, A., Addison, P., Simon, S., & Liuzzo, L. (2023). Data for "A model of Ganymede's magnetic and plasma environment during the Juno PI34 flyby" by Stahl et al., 2023 [Dataset]. Zenodo. <https://doi.org/10.5281/zenodo.8370898>

- Szego, K., Bebesi, Z., Bertucci, C., Coates, A. J., Crary, F., Erdos, G., et al. (2007). Charged particle environment of Titan during the T9 flyby. *Geophysical Research Letters*, 34(24), L24S03. <https://doi.org/10.1029/2007GL030677>
- Tippens, T., Liuzzo, L., & Simon, S. (2022). Influence of Titan's variable electromagnetic environment on the global distribution of energetic neutral atoms. *Journal of Geophysical Research: Space Physics*, 127(10), e2022JA030722. <https://doi.org/10.1029/2022JA030722>
- Tóth, G., Jia, X., Markidis, S., Peng, I. B., Chen, Y., Daldorff, L. K. S., et al. (2016). Extended magnetohydrodynamics with embedded particle-in-cell simulation of Ganymede's magnetosphere. *Journal of Geophysical Research: Space Physics*, 121(2), 1273–1293. <https://doi.org/10.1002/2015JA021997>
- Turc, L., Leclercq, L., Leblanc, F., Modolo, R., & Chaufray, J.-Y. (2014). Modelling Ganymede's neutral environment: A 3D test-particle simulation. *Icarus*, 229, 157–169. <https://doi.org/10.1016/j.icarus.2013.11.005>
- Valek, P. W., Waite, J. H., Allegrini, F., Ebert, R. W., Bagenal, F., Bolton, S. J., et al. (2022). In situ ion composition observations of Ganymede's outflowing ionosphere. *Geophysical Research Letters*, 49(24), e2022GL100281. <https://doi.org/10.1029/2022GL100281>
- Volwerk, M., Kivelson, M. G., Khurana, K. K., & McPherron, R. L. (1999). Probing Ganymede's magnetosphere with field line resonances. *Journal of Geophysical Research*, 104(A7), 14729–14738. <https://doi.org/10.1029/1999JA900161>
- Vorburger, A., Fatemi, S., Galli, A., Liuzzo, L., Poppe, A. R., & Wurz, P. (2022). 3D Monte-Carlo simulation of Ganymede's water exosphere. *Icarus*, 375, 114810. <https://doi.org/10.1016/j.icarus.2021.114810>
- Wang, L., Germaschewski, K., Hakim, A., Dong, C., Raeder, J., & Bhattacharjee, A. (2018). Electron physics in 3-D two-fluid 10-moment modeling of Ganymede's magnetosphere. *Journal of Geophysical Research: Space Physics*, 123(4), 2815–2830. <https://doi.org/10.1002/2017JA024761>
- Weber, T., Moore, K., Connerney, J., Espley, J., DiBraccio, G., & Romanelli, N. (2022). Updated spherical harmonic magnetic field moments of Ganymede from the Juno flyby. *Geophysical Research Letters*, 49(23), e2022GL098633. <https://doi.org/10.1029/2022GL098633>
- Williams, D. J., Mauk, B., & McEntire, R. W. (1997). Trapped electrons in Ganymede's magnetic field. *Geophysical Research Letters*, 24(23), 2953–2956. <https://doi.org/10.1029/97GL03003>
- Williams, D. J., Mauk, B. H., McEntire, R. W., Roelof, E. C., Armstrong, T. P., Wilken, B., et al. (1997). Energetic particle signatures at Ganymede: Implications for Ganymede's magnetic field. *Geophysical Research Letters*, 24(17), 2163–2166. <https://doi.org/10.1029/97GL01931>
- Zhou, H., Tóth, G., Jia, X., Chen, Y., & Markidis, S. (2019). Embedded kinetic simulation of Ganymede's magnetosphere: Improvements and inferences. *Journal of Geophysical Research: Space Physics*, 124(7), 5441–5460. <https://doi.org/10.1029/2019ja026643>